CHAPTER 2

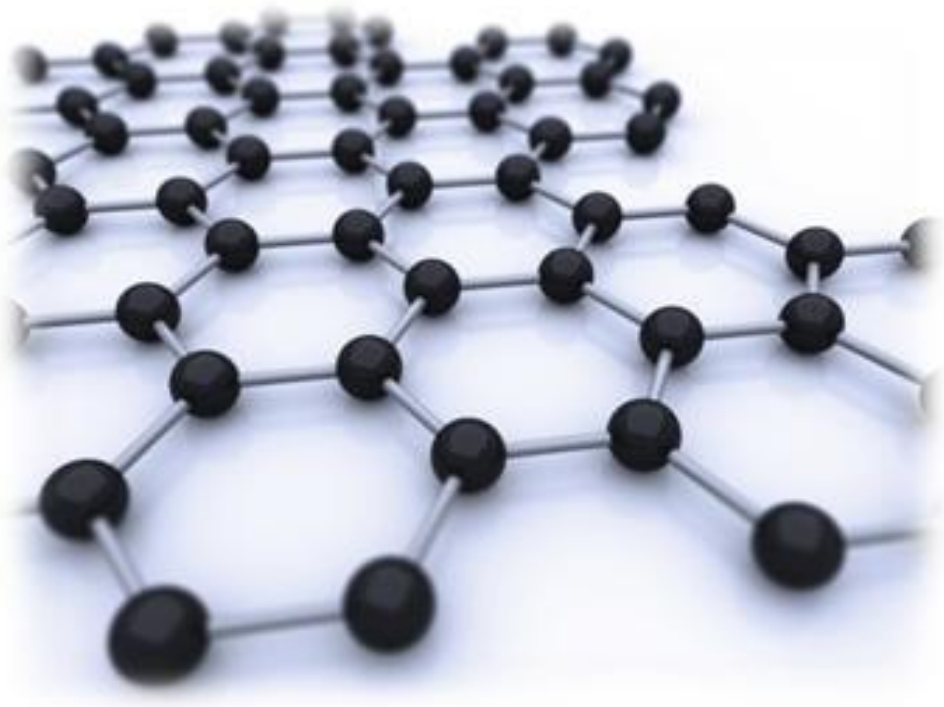

2

Chapter

Literature review

Contents

In this chapter relevant work reported in the literature on photocatalytic dissociation of water have been presented in the literature. This chapter also forms the objectives of the present work.

2.1 Catalysis and photocatalysis

The act of a catalyst on a reaction is called catalysis. A catalyst is a substance that changes the rate of reaction without being consumed in the reaction. In general, catalysts speed up a reaction by decreasing the value of the activation energy by changing the reaction mechanism.

One classification of catalysis on the basis of phases involved in the reaction is: homogeneous and heterogeneous. The reaction in which reactant and catalyst are in the same phase is known as homogeneous catalysis. Examples of homogeneous catalysis are acid-base catalysis, enzyme catalysis. In heterogeneous catalysis reactant and catalyst are in the different phases. Ostwald's process (for making nitric acid) and Haber's process (for the production of ammonia) are examples of heterogeneous catalysis. Metals and semiconductors are used as a catalyst in these reactions, and reaction happens at the interface between the phases [75,76].

"Photocatalysis" was first time introduced in 1930, and frequently used in the literature. Definition for photocatalysis according to IUPAC is "a catalytic reaction involving light absorption by a catalyst or a substrate" [77]. Heterogeneous photocatalysis by semiconductors is a promising field of study. The only difference of photocatalytic reaction with conventional catalysis is the mode of activation. In photocatalysis the thermal activation is replaced by photonic activation.

2.1.1 Semiconductor electrolyte interface [78,79]

This subsection deals with aspects related to electron transfer at semiconductor–electrolyte interfaces. The electrochemical potential of the solution is determined by the redox potential of the electrolyte solution, and the redox potential of the semiconductor is determined by the Fermi level. When a semiconductor is immersed in this redox electrolyte, the electrochemical potential (Fermi level) is different across the interface. Equilibration of this interface thus necessitates the flow of charge from one phase to the other and a ''band bending'' ensues within the semiconductor phase. The excess charges that are now located on the semiconductor do not lie at the surface, but extend to a significant distance. This region is referred to as the space charge region and has an associated electric field. Hence, there are two layers to be considered: first one is interfacial (semiconductor-electrolyte) layer, and second one is space charge layer.

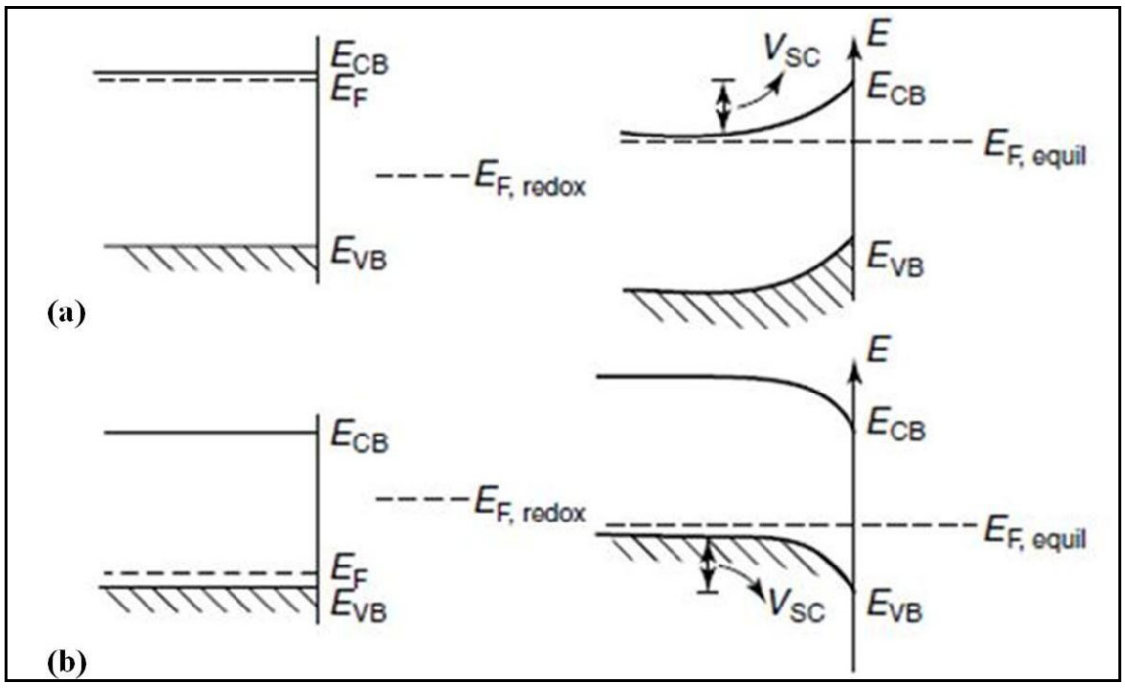

Figure 2.1: (a) The semiconductor-electrolyte interface before (LHS)and after (RHS) equilibration (i.e. contact of the two phases) shown for an *n*-type semiconductor, (b) as in (a) but for a *p*-type semiconductor.

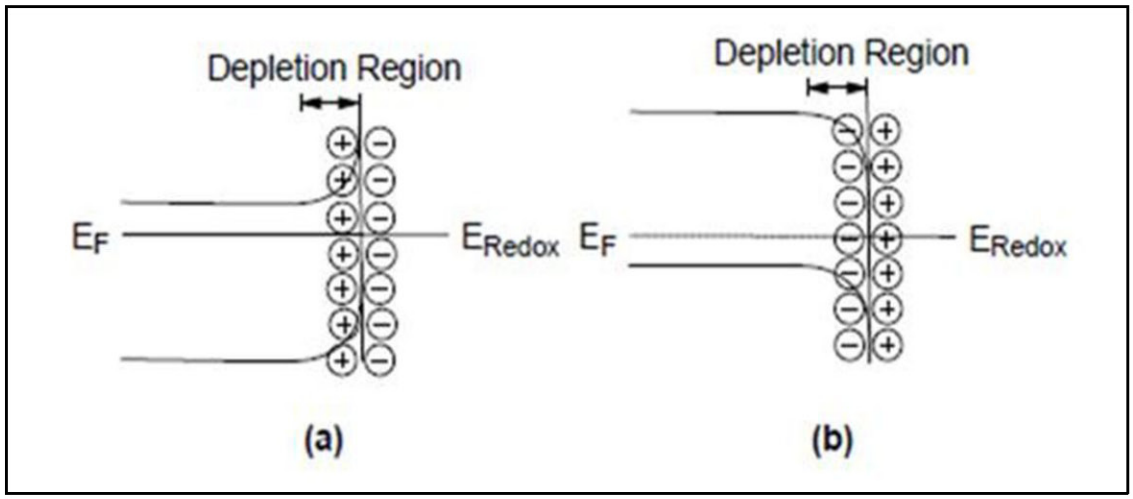

Figure 2.2: Band bending for (a) an *n*-type semiconductor, and (b) a *p*-type semiconductor in equilibrium with an electrolyte.

The situation before and after contact of the two phases are illustrated in Fig. 2.1(a) and 2.1(b) for an *n*-type and *p*-type semiconductor, respectively. After contact, the net result of equilibration is that $E_F = E_{F,redox}$ and a ''built-in'' voltage, V_{SC} develops within the semiconductor phase, as illustrated in the right hand frames of Fig. 2.1(a) and (b). For an *n*-type semiconductor electrode at open circuit, the Fermi level is typically higher than the redox potential of the electrolyte, and hence electrons will be transferred from the electrode into the solution. Therefore, there is a positive charge associated with the space charge region, and this is reflected in an upward bending of the band edges [Fig. 2.2 (a)]. Since the majority charge carrier of the semiconductor has been removed from this region, this region is also referred to as a depletion layer. For a *p*-type semiconductor, the Fermi layer is generally lower than the redox potential, and hence electrons must transfer from the solution to the electrode to attain equilibrium. This generates a negative charge in the space charge region, which causes a downward bending in the band edges [Fig. 2.2 (b)]. Since the holes in the space charge region are removed by this process, this region is again a depletion layer. There are few charge

carriers available for charge transfer, and electron transfer reaction occurs slowly, if there is a depletion layer.

2.1.2 Basic principles of photocatalysis

In general, semiconductors are used as photocatalysts in light induced redox processes [Fig. 2.3].

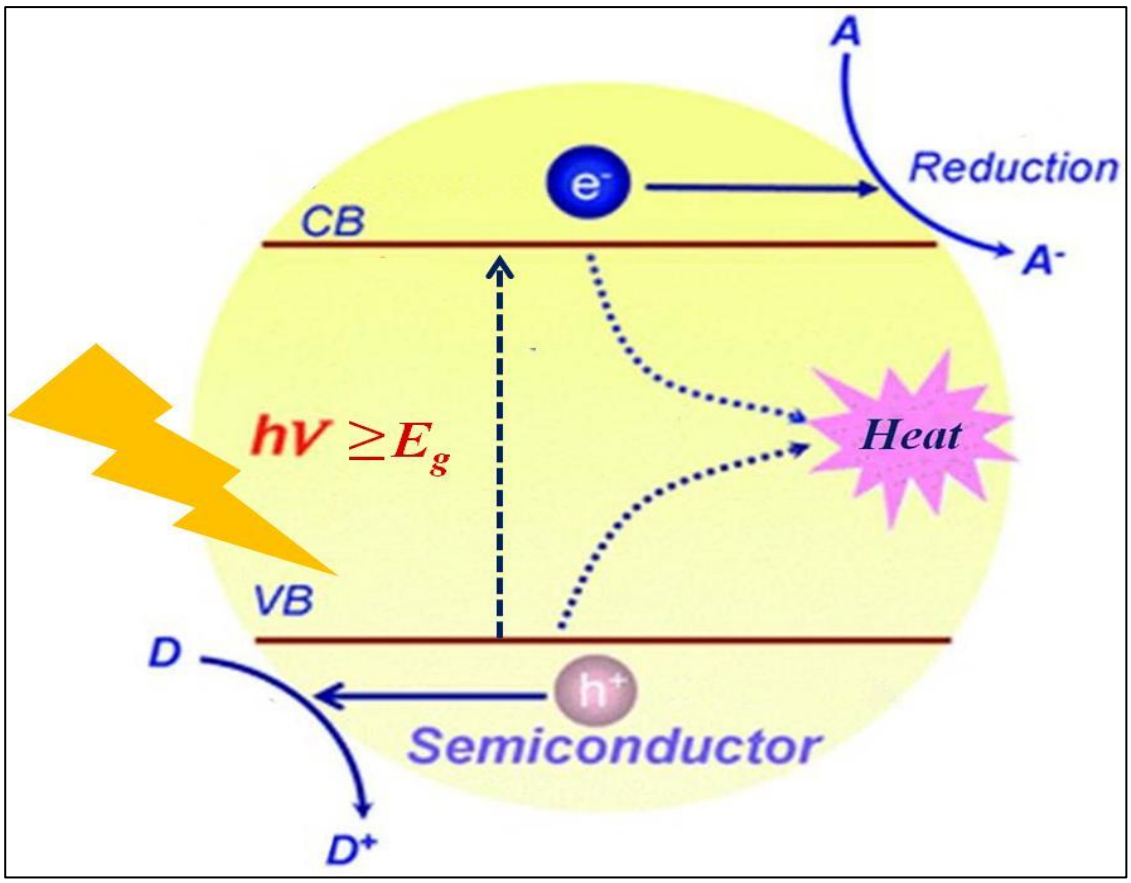

Figure 2.3: Fundamental principle of semiconductor-based photocatalysis (Example: Photocatalytic water splitting for hydrogen production).

Electronic structure of these semiconductors is characterized by a valence band (VB) and conduction band (CB). When a photon (hv) of energy equal to or more than band gap energy (E_g) of the semiconductor falls on it, an electron (e^-_{CB}) jumps from the

VB to the CB and leaves a hole (h^+_{VB}) behind. In this excited state, either, CB electrons and VB holes can recombine and dissipate the energy in the form of heat, or trapped in meta-stable surface states, or react individually with electron donors and electron acceptors present in an electrolyte at the semiconductor interface. Electrons which jump to the conduction band can catalyse reduction of water to hydrogen. Whereas the holes are either utilized for production of oxygen or consumed by some sacrificial agents which get oxidized [details are discussed in section 2.7].

2.2 Hydrogen production by photocatalytic water splitting

Water splitting refers to the dissociation of water molecules to hydrogen and oxygen gases according to Eq^n. 2.1.

$$H_2O\ (l) \rightarrow H_2\ (g) + O_2\ (g) \quad \Delta G_o = 238\ kJ/mol \tag{2.1}$$

$$\Delta G_o = -nFE_0 \tag{2.2}$$

Where, *n* is the number of electrons transferred in the reaction, *F* is the Faraday constant.

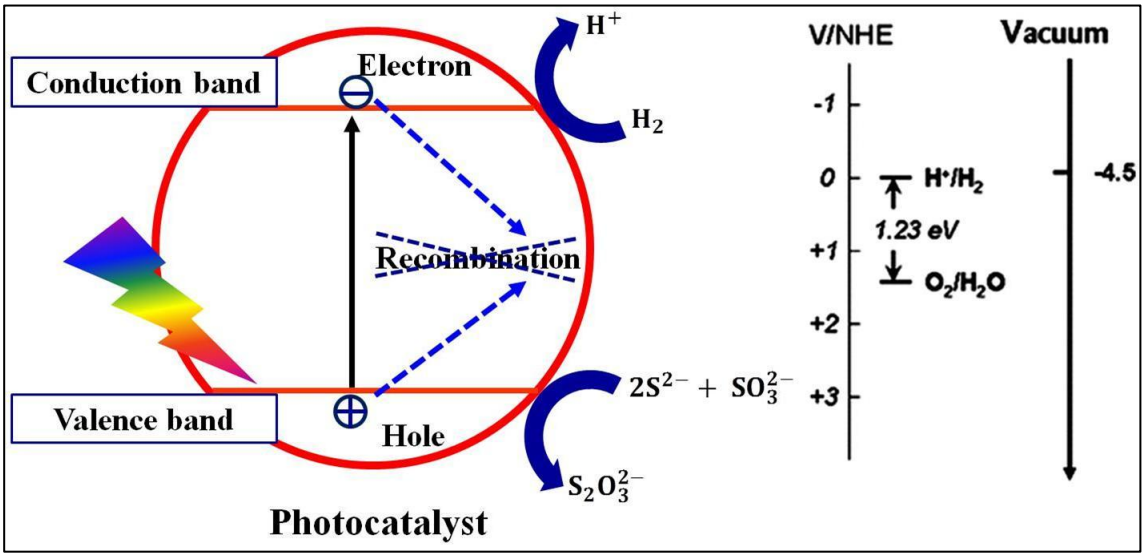

Figure 2.4: Fundamental steps of photocatalytic water splitting for hydrogen production.

Since, the standard Gibbs free energy (at 298 K and 1 atm) is positive the reaction is not spontaneous at room temperature and atmospheric pressure. Energy need to be supplied to carry out the reaction. The minimum energy required per electron will be 1.23 eV, which corresponds to energy of photon of wavelength 1100 nm according to Eq^{n}. 2.3.

$$\mathrm{E} = \frac{1240}{\lambda}\ \mathrm{ev} \tag{2.3}$$

Therefore, the value of band gap energy (E_g) of the photocatalyst should be more than 1.23 eV (<1100 nm) to achieve water splitting.

It means photon of wavelength less than 1100 nm will have sufficient energy to dissociate water. However, water is transparent to UV and visible light, therefore a semiconductor catalyst is required to mediate the process. A semiconductor having narrow band gap where electron-hole pairs are formed due to activation by photons of wavelength less than 1100 nm can act as a catalyst. In addition, the conduction band should be more negative compared to reduction potential of water for electron to carry out the reaction. An electrolyte (typically $SO_3^{2-} + S^{2-}$) gets oxidized by the hole left in the valence band.

The overall water splitting reaction process can be divided into three main steps [as shown in Fig. 2.4]: (i) charge-carrier (electron/hole) generation following absorption of a photon, (ii) charge-carrier separation and migration of electron to conduction band, (iii) reaction between surface species and the charge carriers. The first two steps are photo-physical processes, while the final step is a chemical process. In addition, recombination of electrons and holes may also take place spontaneously. Backward reaction in the liquid phase is also possible. Therefore, research is being carried out for

(a) enhancement in solar light harvesting by developing semiconductors (b) rapid charge separation system and elimination of electron hole recombination. Apart from these, it is also required to make modifications with the material's particle morphology and alter the surface structure modification to increase the reaction rate of redox couples.

2.3 Photocatalysts for water splitting

This subsection summarizes the active photocatalysts well reported in the literature. It also includes reported works on band gap engineering and various schemes for the operation of photocatalytic system.

Historically, Fujishima and Honda reported hydrogen production by using a TiO_2 single crystal electrode from photocatalytic water decomposition [80]. They reported the processes in which solar energy could be transformed into chemical energy directly. Subsequently, more studies have been conducted on the photocatalytic dissociation of water as a clean solar energy conversion process leading to a non-polluting fuel. Excellent reviews on this topic have been published by Tentu et al. [81], Preethi et al. [82], Tee et al. [83], Osterloh et al. [84], Ismail et al. [85], Rao et al. [86], Kudo et al. [87, 88], and Kazunari et al. [89].

Literature reports various photocatalysts developed and studied for photocatalytic H_2 productions. They exhibit good photocatalytic activities. However, many of them could be activated by the UV light only. Since, more than 40% part of the solar radiation spectrum coming on the earth surface is the visible, less than 5% is near ultraviolet and remaining is of near-infrared range [Fig. 2.5], therefore, the utilization of visible light in various chemical reactions is very attractive. It is, therefore, crucial to

develop visible light driven photocatalysts that are stable and highly efficient for the realistic, large scale production of hydrogen using solar energy.

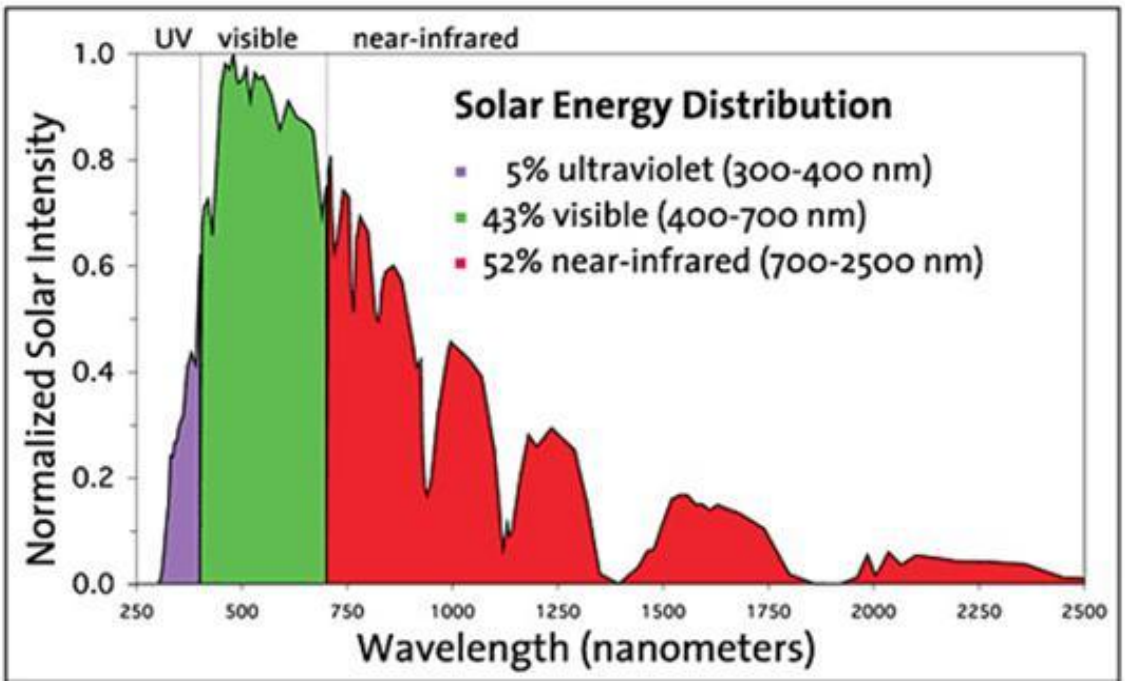

Figure 2.5: Solar energy distribution.

Generally, photocatalysts can be classified as metal oxide, sulphide and nitride.

2.3.1 Metal oxide photocatalysts

Water splitting photocatalysts are mainly those transition metal oxides containing metal cations with d^0 and d^{10} configurations. The d^0 metal oxides are from IVB group (Ti^{4+}, Zr^{4+}), VB group (Nb^{5+}, Ta^{5+}) and VIB group (Mo^{6+}, W^{6+}) while the d^{10} metal oxides are from IIIA group (Ga^{3+}, In^{3+}), IVA group (Ge^{4+}, Sn^{4+}) and VA group (Sb^{5+}).

TiO_2 i.e., group IVB metal oxides[90], has been widely investigated photocatalyst for water splitting reaction. However, TiO_2 has a large band gap; and is

active under ultraviolet light only. Till now, a various approaches have been adopted by researchers to synthesis TiO_2-based photocatalyst for H_2 production under visible light irradiation. Doping of photocatalysts to produce a visible light response is one of the most commonly reported approaches to improving the visible light activity. A few common approaches for doping reported in the literature are:

- Non-metal ions doping for band gap narrowing
- Metal ions doping for band gap narrowing
- Metal/Non-metal ion codoping

(a) Non-metal ions doping for band gap narrowing

Recently, doping by non-metal ions has been shown to be a promising approach in which the semiconductor absorption threshold is shifted into the visible region [91] [Fig. 2.6]. In particular, oxygen is partially substituted by non metal elements, such as nitrogen [92–94], carbon [95,96], sulphur [97,98], and boron [99,100] in semiconducting oxides, and further these should produce infra band gap electronic states, thus inducing a red-shift of the absorption threshold. For example Asahi et al. [92] reported doping of various non-metal elements such as C, N, F, P, and S to substitute O with these in TiO_2. It was found that mixing of p states of N with 2p of O could shift the VB edge upwards to narrow down the bandgap of TiO_2. Umebayashi et al. [101] reported that when TiO_2 was doped with S, the mixing of S 3pstates with the VB of TiO_2 increased the width of VB, resulting in bandgap narrowing. Burda et al. [93] reported doping of nitrogen up to 8% with TiO_2. The synthesized N doped $TiO_2$was visible light active and absorbed well into the visible region up to 600 nm. Wu et al. [102] and Luo et al. [103] reported doping of halides as F, Cl and Br into TiO_2. This doping increased the optical response in visible spectral region. Dozzi et al. [91]

presented overview of non-metal ion doping with TiO_2. Although light absorption was shifted into visible range after the introduction of doping, but visible-light photocatalytic activities were not satisfactory compared to activity found under UV irradiation. Furthermore, another problem was higher recombination rate of the charge carriers in doped samples. These problems were partly reduced by co-doping [104,105].

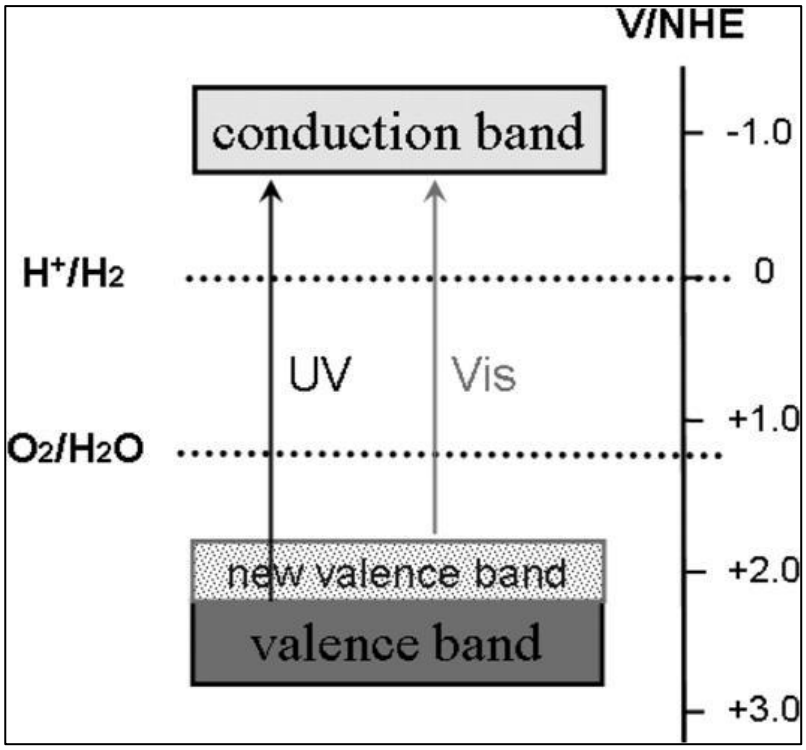

Figure 2.6: New valence band formation by doping of nonmetal ions [106].

(b) Metal ions doping for band gap narrowing

Another approach i.e. similar to previous one is metal ion doping in which the adsorption threshold is shifted towards the visible region. It is an effective method to develop visible light driven photocatalyst. Impurity levels were formed in the forbidden band gap [Fig. 2.7]. This approach has been known for a long time. Several examples

were reported using V, Ni, Cr, Mo, Fe, Sn, Mn, Co, Rh etc metals doped materials [107–112]. For example, Choi et al. [108] studied the photoactivity of various metal ions doped into TiO_2. They reported that doping of metal ions could expand the photo-response of TiO_2 into visible-light spectrum. As metal ions were incorporated into the TiO_2 lattice, impurity energy levels in the bandgap of TiO_2 were formed. Xu et al. [113] also reported the comparison in photocatalytic activities of different rare earth metal ions (La, Ce, Er, Pr, Gd, Nd and Sm) doped TiO_2 with undoped TiO_2. Enhanced photocatalytic activities and red shift of photo-response were observed at certain doping content.

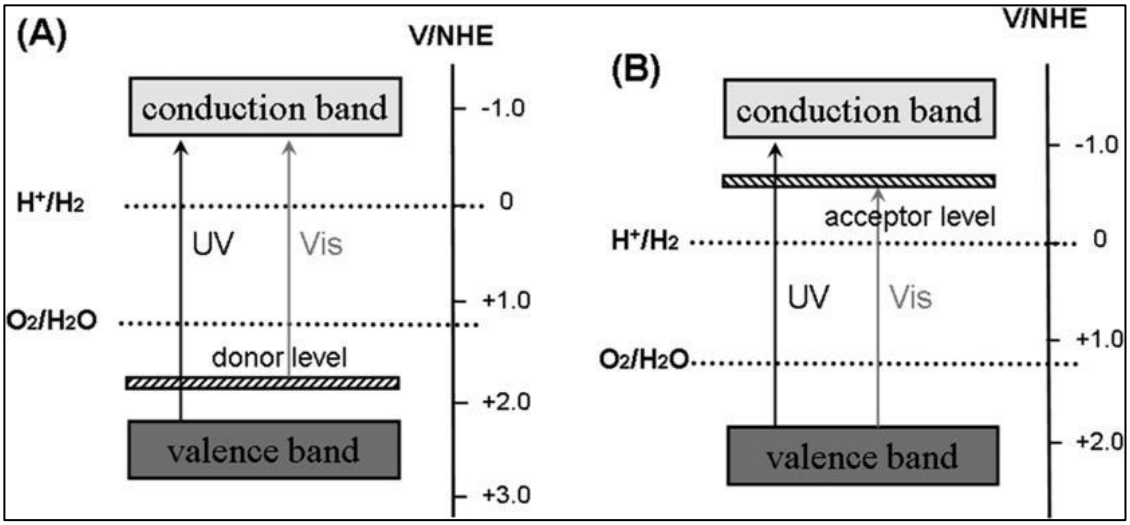

Figure 2.7: Donor level (A) and acceptor level (B) formed by metal ion doping [106].

The benefit of metal doping species is better capability of trapping electrons to inhibit electron-hole recombination also over non-metal doping. Moreover, non-metal ions doping formed lesser donor levels in the forbidden band.

(c) Metal/non-metal ion co-doping

To fulfil the objective of improving their hydrogen production activity by photocatalysis by harvesting visible light, metal/non-metal ion co-doped semiconductor systems have been employed as photocatalysts. The modification of various photocatalysts with co doping ofCe + (C, I, N, B), Fe + (C, N), Ni + (B, N etc) used to improve the photocatalytic activity [114–116]. Sashikala et al. [115] reported codoping of TiO_2 with N and In, resulted enhanced absorption of visible light and improved photocatalytic activity. Gai at al. [116] reported modification of band edges of TiO_2 by codopants (Mo+C) to shift the valence band edge up significantly resulted enhanced photocatalytic activity. Very few studies were reported on metal/non-metal ion codoped photocatalysts.

2.3.2 Metal sulphide photocatalysts

Metal Sulphide photocatalysts have been studied more for hydrogen production. Conduction bands of these semiconductors are more negative which are favourable for dissociation of H_2O into H_2 [117]. Moreover, these sulphides based photocatalysts are more responsive to solar light compared to oxide based photocatalysts. Sacrificial reagents are always needed to achieve photocatalytic hydrogen production [discussed in section 2.7]. For example, sulphides always exhibit excellent photocatalytic activities in aqueous solution using Na_2S and Na_2SO_3 as sacrificial reagents [118]. In the past few decades, various metal sulphide photocatalysts have been reported for H_2O dissociation in the presence of different sacrificial reagents. Generally, most of the metal sulphides photocatalysts consist of metal cations with d^{10} configuration (e.g. group IB: Cu, Ag; group IIB: Zn, Cd; group IIIA: Ga, In; group IVA: Ge, Sn) [117,119]. Therefore, the CBs of sulphide semiconductor are composed of d and sp orbitals with the valence

bands consisting of S 3p orbitals. These S 3p orbitals are more negative than O 2p orbitals resulting in more negative positions of conduction band that is enough to reduce H_2O into H_2 and narrow band gaps with suitable response to the solar spectrum. ZnS [120–124], CdS, and CdSe [125–128] i.e. Group IIB chalcogenides are most studied photocatalyst.

CdS is probably the best-studied metal sulphide photocatalyst for H_2 evolution, because of its narrow band gap (2.4 eV) [129] that suits very well with the solar spectrum and good band positions for reducing H_2O to H_2. So it fulfils the requirement of ideal photocatalyst except one major drawback, which is separation of photogenerated charges [130–133].

2.4 Charge recombination phenomena and its prevention

The photogenerated electrons and holes need to be separated and be available for chemical reaction. Else they will recombine and produce heat or radiation only. The recombination of photo-induced electron is too rapid compared to its migration to surface and split water. In general, time for recombination~1×10^{-9} [134] second is ten times faster than the time taken for chemical reaction. It has been reported that 70% of photogenerated carriers recombine after excitation and due to this major problem photocatalytic efficiency is not achieved as required. Clearly, the photogenerated charge carriers must be efficiently separated in order to enhance the utilization rate of the charge carriers by transferring to the active sites on photocatalysts surface and achieve high hydrogen production rate by photocatalytic water splitting.

The literature reports [135–137] use of cocatalysts usually a noble metal or metal oxide or a combination of them to form heterojunction, which are embedded on the

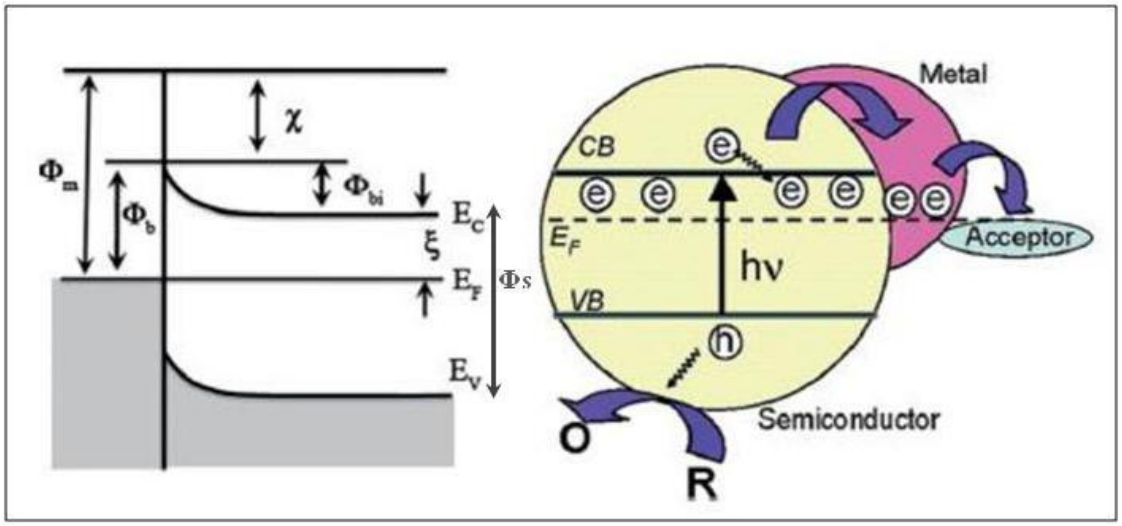

Figure 2.8: Metal/semiconductor Schottky junction with energy level equilibration. **(Left)**, processes of charge transfer in charge separation between host photocatalyst and cocatalyst (Pt) (**Right).** E_F-Fermi energy, E_v-valence band position, E_c- conduction band position, Φ_m- work function of metal, Φs – semiconductor band gap, ε = Difference between Fermi level and conduction band position of semiconductor, $\Phi_b = \Phi m - \Phi s$, Φ_{bi} = barrier potential created due to Schottky junction.

surface of host photocatalyst to enhance the photogenerated charge separation [Fig. 2.8]. Generally, noble metals have higher work-function compared to semiconductor photocatalysts. Platinum is the most commonly used co-catalyst for this purpose. Loading of noble metal on the surface of a semiconductor forms the Schottky barrier [Fig. 2.8]. Schottky barrier is also called a space-charge separation region. It is created at semiconductor–metal junction. The work function of the metal (Φ_m) is higher than that of the semiconductor (Φ_s) and electrons will flow from the semiconductor into the metal to align the Fermi energy (E_F) levels at the heterojunction (interface) [Fig. 2.9]. Schottky barrier can serve as an efficient electron trap preventing electron–hole recombination in photocatalysis, which often results in an enhanced photocatalytic performance. In the Fig. 2.9, Φ_b represents the height of the potential barrier, which depends on the band bending of the semiconductor and the Fermi level of metal. This is called the Schottky barrier Φ_b.

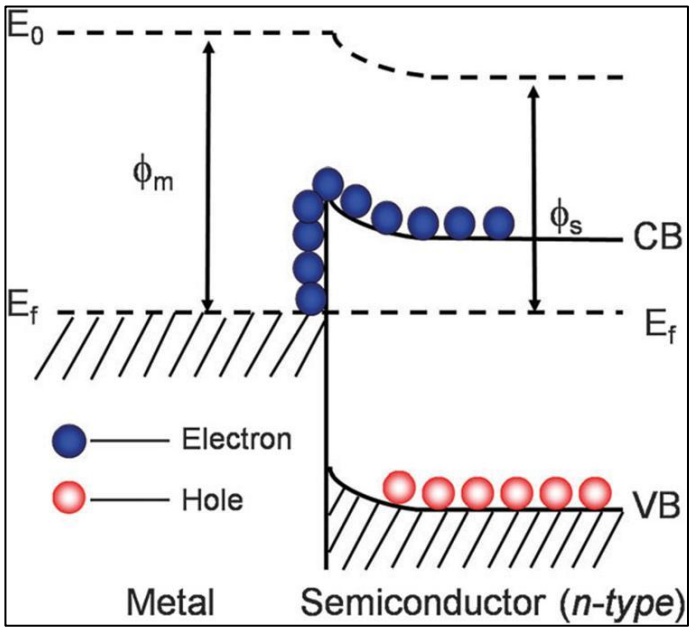

Figure 2.9: Schematic of the Schottky barrier [138].

Therefore, noble metal cocatalysts have been widely applied for the enhancement of photocatalytic activities. The most commonly used metals are Pt [132,139–141], Pd [142,143], Au [144,145], and Rh [146]. Among them, Pt is the most popular one owing to its low Fermi level and it has been considered to be effective in inhibiting photogenerated charges recombination

Another approach to improve its photocatalytic activity and stability is to make a composite of two or more semiconductors embedded with other semiconductors of suitable band energies. Literatures suggest that a combination of two semiconductors provides a heterojunction which may be effective for charge separation. When the *p*- and *n*-type semiconductors are in contact [Fig. 2.10], a *p*–*n* junction may form with a space-charge region at the interfaces due to the diffusion of electrons and holes. Thus a built-in electrical potential is created and the electrons& holes can directly travel in the opposite direction due to this potential. When the *p*–*n* heterojunction is irradiated by

photons with energy higher or equal to the bandgap of the photocatalyst, the photogenerated electron–hole pairs can be quickly separated by the built-in electric field within the space charge region. Several advantages can be obtained in this *p–n* heterojunction: (a) a more effective charge separation; (b) a rapid charge transfer to the catalyst; (c) a longer lifetime of the charge carriers. All of these features give the *p–n* heterojunction with an enhanced photocatalytic performance.

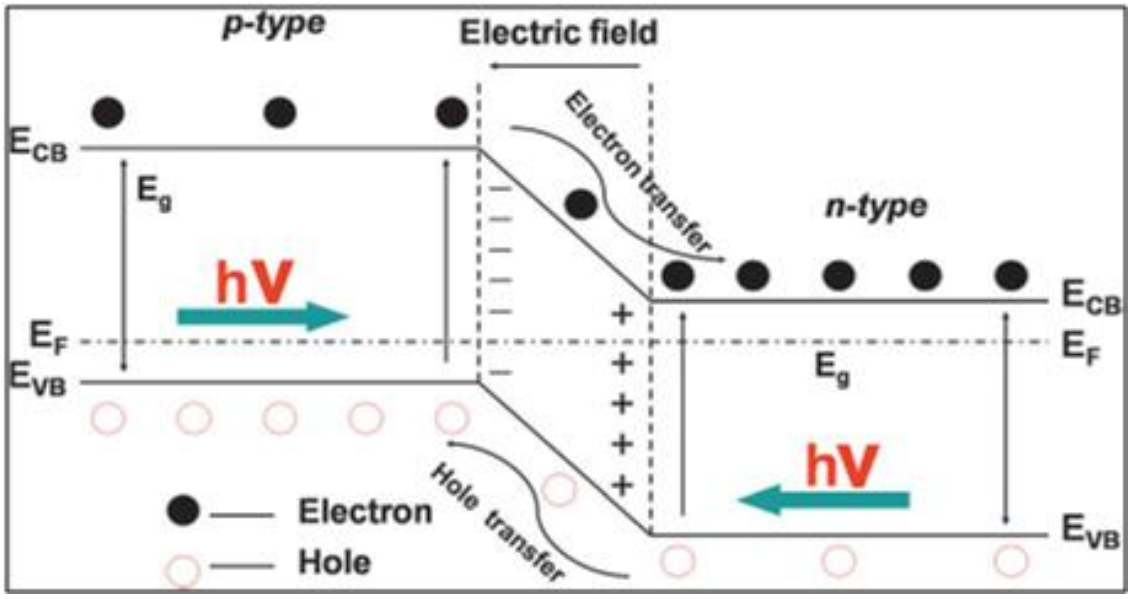

Figure 2.10: Schematic diagram showing the energy band structure and electron–hole pair separation in the p–n heterojunction [138].

In addition to the *p–n* type heterojunction, non-*p–n* type heterojunction systems may also form [Fig. 2.11]. In this type, the semiconductors A and B with matching band potentials are tightly bonded to construct the efficient heterojunction. When the CB level of semiconductor-B is lower than that of semiconductor-A, electrons in the CB of semiconductor-A can be transferred to that of semiconductor-B. If the VB level of semiconductor-B is lower than that of semiconductor-A, holes in the VB of

semiconductor-B can be transferred to that of semiconductor-A. As a result, the separation and migration of photogenerated carriers can be promoted by the internal field, and the probability of electron–hole recombination can be reduced. A larger number of electrons on the semiconductor-B surface can participate in photocatalytic reactions and thus the photocatalytic rate can be enhanced greatly.

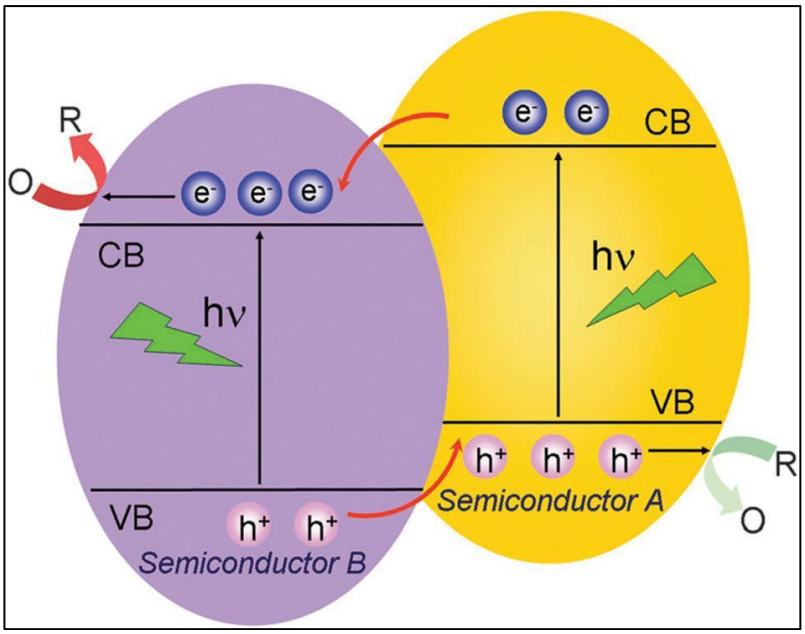

Figure 2.11: Schematic diagram showing the energy band structure and electron–hole pair separation in the non-*p*–*n* heterojunction [138].

Among these composites, CdS/TiO_2 [147–149] has been taken as an example as shown in Fig. 2.12. A photogenerated electron gets transferred from conduction band of TiO_2 to that of another semiconductor CdS. Under visible-light irradiation, the photogenerated electrons in the CdS particle are quickly transferred to TiO_2 particles, whereas photogenerated holes stay in CdS. This facilitates the electron−hole separation and prevents the charge recombination, improving the photocatalytic activity.

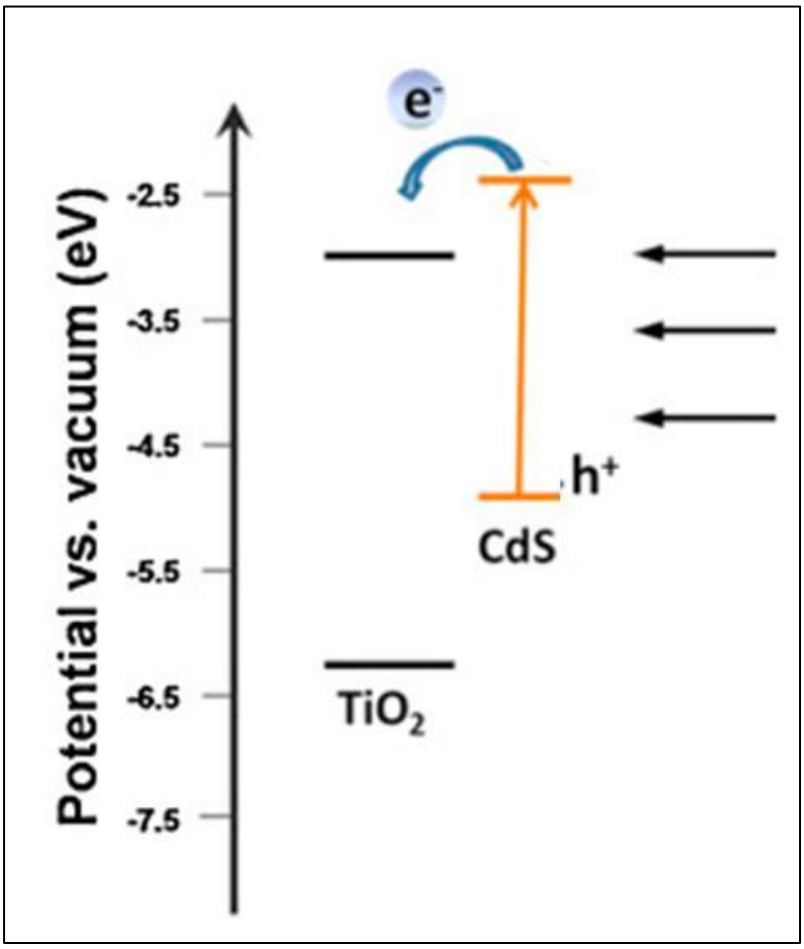

Figure 2.12: Processes of charge transfer (charge separation) between host photocatalyst and another semiconductor in mixed semiconductor combination system.

Since in the present work we have focused on CdS based catalysts, in the following pages we discuss the literature related to this catalyst. A number of workers have reported work on CdS photocatalyst. Both the techniques, i.e., metal deposition and composite with another semiconductor have been attempted to enhance activity. A few selected works have been listed in the Table 2.1. A comparison of activity shows wide variation because experiments were carried out with different experimental set-up, experimental condition and light sources. From the review of the reported work, it can be concluded that sacrificial reagents are essentially required for CdS-based

photocatalysts to satisfy holes to prevent photocorrosion of CdS [discussed in section 2.7]. It also prevents simultaneous formation of O_2 [referred to section 2.7]. Moreover, cocatalysts are also required to improve the activity for hydrogen production.

A variety of combinations of CdS, TiO_2, and Pt in preparing the hybrid catalysts were studied by Park et al. [150] for hydrogen production under visible light ($\lambda > 420$ nm) irradiation. They reported that after the using of Pt as a cocatalyst, activity increased which was higher by a factor of 3thanthat of CdS/TiO_2. Jang et al. [151] have also reported that platinized CdS/TiO_2photocatalysts showed higher hydrogen production from water compared to binary mixture of CdS and TiO_2. Daskalaki et al. [152] also reported solar light-responsive Pt/CdS/TiO_2photocatalysts for enhanced hydrogen production compared to binary composites.

Therefore, photocatalysts loaded with the cocatalyst Pt are the most efficient and higher H_2 production photocatalytic activity by dissociation of water utilizing visible light irradiation. However, Pt is costly as well as scarce metal, so attention is shifting to find some alternative having same or a better efficiency. In this context, Graphene has been widely studied. It behaves like metals with a high work function [153]. The work function of graphene is 4.42 eV. Moreover, the reduction potential of graphene is reported to be –0.08 eV vs. NHE at pH = 0 [Fig. 2.13], it is less negative than that of the CdS CB level (–0.52 V vs. NHE) [154], thus leading to the thermodynamically easier transfer of the photogenerated electrons from CdS to graphene [155,156]. It has high electron conductivity which may facilitate a quick transfer of electron to the solid liquid interface. Therefore, graphene seems to be a promising substrate that can replace noble metals to present cost effective cocatalyst option.

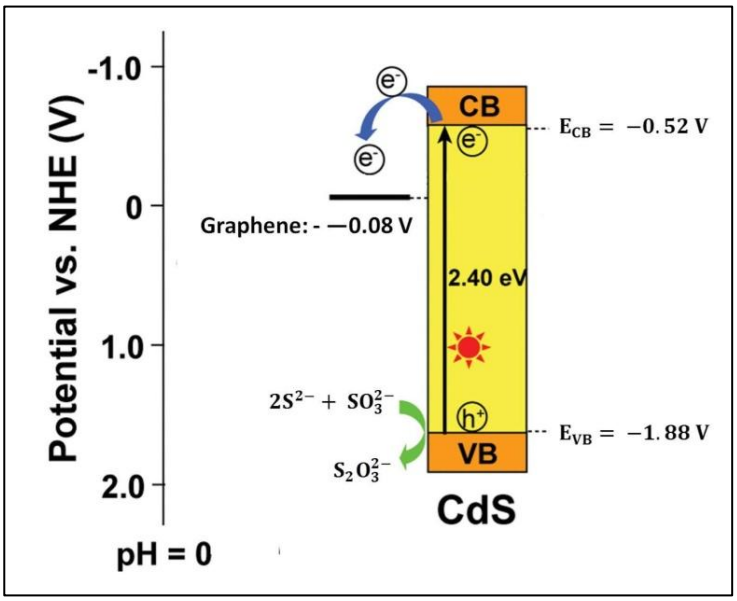

Figure 2.13: Reduction potential of graphene [155,157].

Table 2.1: List of CdS based photocatalyst for hydrogen production by dissociation of water under visible light

Sr.	System / Co-Catalyst	Preparation Method	Sacrificial Agent	Production ($\mu mol.h^{-1}$)	Ref
1.	CdS/**Rh**	Purchased	Na_2SO_3	185	[146]
2.	CdS/**Pt**	Physically Grinded	Na_2SO_3	1680	[140]
3.	CdS/**Pt**	Physically, Cubic CdS on Hexagonal CdS	Na_2SO_3, Na_2S	668	[158]
4.	CdS/**MoS_2**	Precipitation	Lactic acid	5200	[159]
5.	CdS/**Pt**	Precipitation	Na_2SO_3, Na_2S	13860	[160]
6.	CdS/**Pt-PdS**	Precipitation	Na_2SO_3, Na_2S	29233	[132]
7.	CdS/**WC**	Precipitation/Hydrothermal	Na_2SO_3, Na_2S	1350	[161]
8.	CdS/**Pt**	Thermolysis	Na_2SO_3, Na_2S	83.3	[162]

9.	CdS/**Pt**	Polymer Inorganic Solid State Reaction	KOH	7856	[163]
10.	CdS/**Pt**	Thermal sulphidation	Na_2SO_3, Na_2S	5625	[164]
11.	CdS/Al-HMS/**Ru**	Ion-exchange	Formic Acid	825	[165]
12.	Alumina/CdS	Impregnation Method	Na_2SO_3, Na_2S	180.8	[166]
13.	Alumina/CdS	Impregnation Method	Na_2SO_3, Na_2S	41.3	[167]
14.	Alumina/CdS	Impregnation Method	Na_2SO_3, Na_2S	90.4	[168]
15.	Incorporated on Special Glass	Two step thermal sulphidation method	Na_2SO_3, Na_2S	1549	[169]
16.	CdS/$LaMnO_3$	Reverse micelle method	None	595	[170]
17.	Ni/NiO/$KNbO_3$	Solid state reaction	Isopropanol	150	[171]
18.	CdS/PANI	Precipitation Method	Na_2SO_3, Na_2S	300	[172]
19.	CdS/SrS	Co precipitation Method	Na_2SO_3, Na_2S	615	[173]
20.	CdS/TiO_2/**Pt**	Precipitation & Sol-Gel Synthesis	Na_2SO_3, Na_2S	6400	[174]
21.	CdS/TiO_2/**Pt**	Two Step Method	Na_2SO_3, Na_2S	4224	[175]
22.	CdS/Zn/Ti/**Pt**	Two Step thermal Sulphidation method	Na_2SO_3, Na_2S	2300	[176]
23.	In doped CdS on ZrO_2/**Pd**	The Polyol Method	Na_2SO_3, Na_2S	800	[177]

2.5 Graphene: Background and current status

Graphene, a new two-dimensional carbon material, is a promising substrate having zero bandgap. Basically, the CB (π*-state) and the VB (π-state) of graphene meet at six points and these are also called Dirac points [178], as shown in Fig 2.14. The band structure of graphene is symmetric about the Dirac point with the Fermi level located between VB and CB. As a result, graphene behaves as zero-band gap material or semi-metal. With this exclusive band structure graphene shows high conductivity that is essential for high electron mobility. Furthermore, the band structure of graphene can be tailored by heteroatom doping resulting in the shift of Fermi level and also shift in Dirac point. Subsequently, graphene shows *n*-type or *p*-type semiconductivity with a small bandgap [Fig 2.15] [179–181].

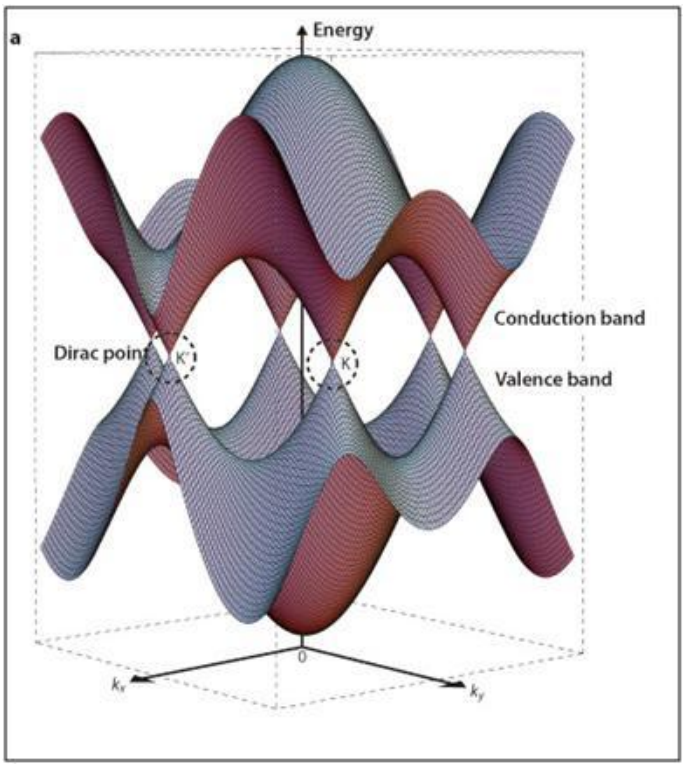

Figure 2.14: Typical **e**nergy band and structure of graphene.

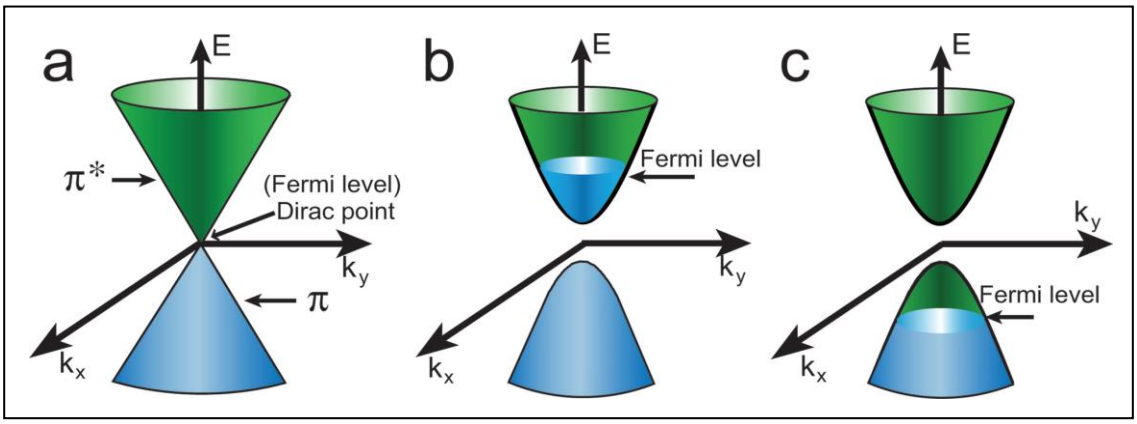

Figure 2.15: (a) Energy band and structure of graphene; Shifting from Dirac point - Energy band structure of b) *n*-type and c) *p*-type graphene by suitable heteroatom doping [178].

Doping by oxygen is most common and the resulting material is called Graphene oxide (GO). Doping with oxygen results into structural deformation due to formation of sp^3 C–O bonds damaging the conductive π-network. This doping may be obtained by chemical exfoliation of graphite through oxidization [Fig. 2.16]. It renders graphene with various oxygen containing functional groups [182–185]. These groups are epoxy, carboxyl or hydroxyl attached on edges as well as basal plane. GO shows insulator properties due to the formation of sp^3 hybridized carbon atoms which interrupt the delocalized π-conjugation. The intrinsic electronic and structural properties of graphene can be modified by reduction of GO. However, experiments have shown that even after reduction, a number of oxygen groups and defects still remain. For these reasons, a separate term for the product is used i.e. reduced graphene oxide (rGO). Thus the reduced graphene oxide behaves like a semiconductor with excellent electron conductivity.

The chemical functionalization can also be applied on GO to tune its electronic properties [182,186]. The carbon–oxygen bonds on graphene leads to

the change of electronic states and the formation of a larger band gap. Carbon–oxygen covalent bonds break the extended sp^2 conjugated network, and confine the original π–electrons within the isolated sp^2 domains. Although, the CB minimum is still composed of the anti-bonding π^*–orbital, while the valence band maximum is formed by the O2p orbital instead of the π–orbital of graphene. So, it is known that GO/rGO with additional oxygenated components is a *p*–type semiconductor [187,188]. Oxygen groups present in rGO give rise to the abundant active sites on the surface which are in the form of dangling oxygen bonds, vacancy defects and sites of localized orbital. These active sites where functional groups may be attached of chemical interaction may take place as a precursor in graphene–based composite.

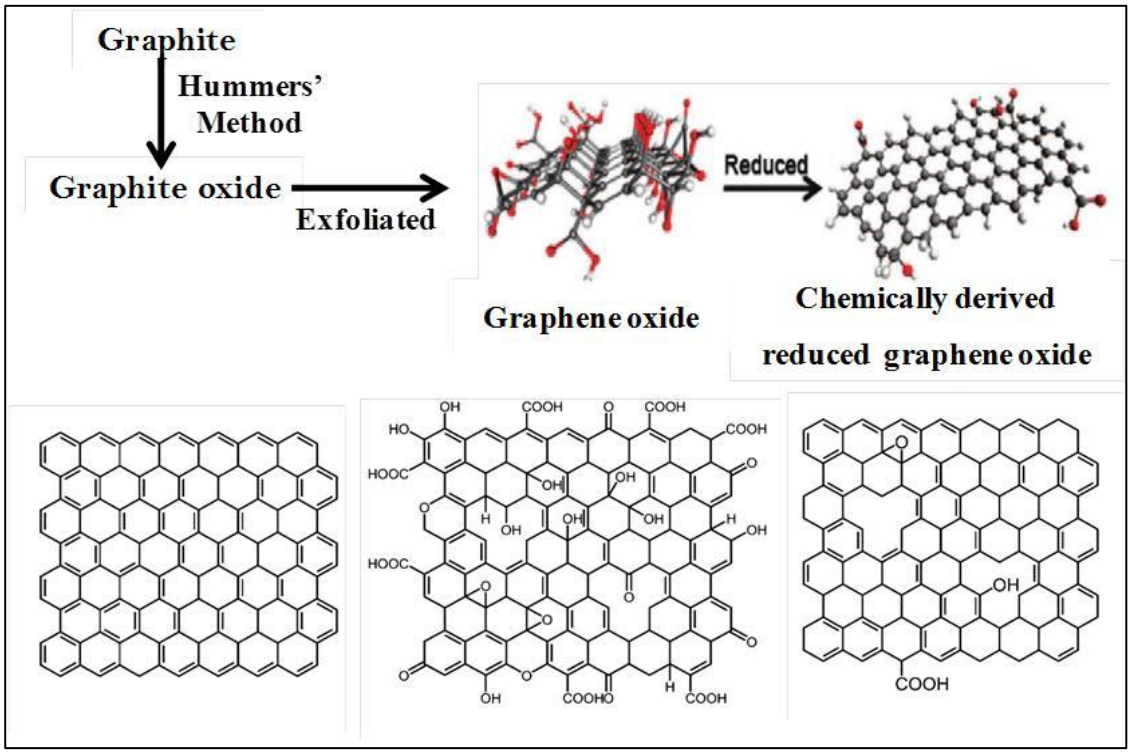

Figure 2.16: Schematic diagram of the synthesis of the graphite oxide, GO, rGO.

Thus the reduced graphene oxide behaves like a semiconductor with excellent electron conductivity. Because of these two desirable properties, GO and rGO have been investigated as co-catalyst in photocatalytic decomposition of water.

2.6 GO/rGO-CdS based photocatalysts

In the following pages, we discuss recent work reported on GO/rGO based CdS photocatalysis.

Various review articles [189–191] have been published to demonstrate the roles of graphene in photocatalytic hydrogen generation. These provide a comprehensive overview of the recent research progress on graphene-based materials for hydrogen evolution from light-driven water splitting. Various catalyst systems have been prepared by different techniques with enhanced actively compared to bare CdS [Table 2.2]. The widely used preparation methods are in situ growth, solution mixing, hydrothermal and/or solvothermal method. The following paragraphs will give a more detailed description of the available synthesis routes.

2.6.1 In-situ growth strategy

The direct growth strategy is widely used to prepare graphene based-metal sulphide composites. The most common precursors of graphene and metal compound are functional GO and metal salts, respectively. Usually, the salt is mixed with GO and then converted to the corresponding sulphide, forming a GO/metal sulphide composite. GO was reduced during composite preparation, and then graphene based-metal compound composites were produced. Cao et al. [192] prepared graphene/CdS composite by a one-step method. In this process, GO and $Cd(CH_3COO)_2.2H_2O$ were

dissolved into DMSO where, DMSO released H_2S during this one-step reaction. It acted both the reducing agent of GO as well as the sulphide source. Thus, simultaneously deposition of CdS and the reduction of GO occurred on the graphene. It produced a single-layer graphene–CdS quantum dot nanocomposite and a uniform distribution of CdS nanoparticles having size of 10 nm on graphene sheets.

2.6.2 Two-phase method

Gao et al. [193] reported GO–CdS synthesis by the two-phase method, first CdS was prepared by mixing solution of cadmium chloride hydrate & sulphur into oleylamine and then heated at 433 K in N_2 atmosphere under constant stirring. Finally CdS was dispersed in toluene with as prepared GO. The morphology and structure of nano-composite was investigated by AFM, TEM, XRD, FTIR and XPS spectroscopy, confirming the good deposition of CdS and on GO sheets. It contributed to the effective hydrogen evolution due to high light harvesting ability and efficient charge transfer. GO–CdS shows much higher hydrogen evolution activity than CdS i.e. four times higher.

Tonda et al. [194] reported the synthesis of g-C_3N_4CdS/rGO ternary composite. Initially, the binary g-C_3N_4/CdS composite was synthesized in which the synthesized g-C_3N_4 nanosheets were dispersed in methanol/water (1:1 volume ratio) solution under ultrasonication for 0.5 h. A required amount of CdS nanorods was then added to the dispersion and ultrasonicated for another 0.5 h. This suspension was continuously stirred for 12 h. Subsequently, the suspension was collected by centrifugation, washed with water and ethanol, and then dried at 353 K. The product was heated at 573 K

for 2 h under N_2 atmosphere. Further rGO was mixed in methanol/water (1:1 volume ratio) solution and ultrasonicated for 1 h. After that, the above synthesized g-C_3N_4/CdS powder was added to the suspension and ultrasonicated for 0.5 h to form a uniform dispersion. Finally, after continuous stirring for 3 h, the suspension was collected by centrifugation and washed with water and ethanol, and then dried at 353 K. It was reported that the CdS nanorods on the surface of g-C_3N_4 were almost covered by rGO sheets and sandwiched between g-C_3N_4 and rGO sheets to form g-C_3N_4/CdS/rGO ternary heterojunctions. Therefore, g-C_3N_4/CdS/rGO exhibits the highest H_2 production rate, which is almost eleven times higher than that for the binary g-C_3N_4/rGO and more than 2 times that for the binary g-C_3N_4/CdS systems.

Jia et al. [195] prepared CdS–graphene samples by mixing CdS nanoparticles, graphene oxide (GO) in ethanol, followed by sonication for 2 h and stirring for 24 h at room temperature. Graphene was first synthesized by an improved Hummers' method. CdS was separately synthesized. CdS–graphene gave the highest H_2 evolution rate of 3.067 mL h^{-1}, which is about 5 times higher than that of CdS. XRD and TEM had ruled out any new phase formation in this mixture during preparation. Improved hydrogen production was attributed to a high degree of light harvesting ability and effective charge transfer between these two nanomaterials through the 2D graphene structure.

Khan et al. [196] prepared GO loaded CdS/Al_2O_3 and CdS/ZnO by solid state route. Briefly, 0.2 g of as prepared CdS/Oxide was thoroughly ground with 1 wt% of as prepared GO using a mortar and pestle for 0.5 h. The rationale behind the grinding of CdS/Oxide and GO was to make uniform contact between them. The obtained powder

was used to examine the effect of GO on the photocatalytic activity of CdS/Oxide. The high photocatalytic activity of CdS/Oxide/GO was attributed to the sheet like structure of graphene oxide which provides a large surface area for effective mass transfer and facile charge transfer that reduces the recombination rate of photoinduced charge carriers.

2.6.3 Sol gel method

Jia et al. [197] studied N-graphene-CdS photocatalyst. It was prepared by adding cadmium chloride into GO solution of ethanol. Na_2S solution was added drop-by-drop into the suspension with stirring, washed and finally heated in nitrogen atmospheres at 673 K for 2 h. The hydrogen evolution rate of CdS was significantly enhanced by loading N-doped graphene. A H_2-production rate was 210 mmol.h^{-1} exceeding that on pure CdS (40 mmol.h^{-1}) by more than 5 times. The enhanced H_2evolution was attributed to the predominant electrical conductivity of N-graphene, indicating that the photoinduced electrons transport to the surface of the composites much easily to prevent there combination between photogenerated electrons and holes. They also reported that crystallinity, morphology, surface area (particle size), and band gap energy between N-graphene/CdS and CdS were not responsible for the remarkable enhancement of H_2 production.

Lv et al. [198] prepared CdS–graphene oxide. In this process, first sulphonated graphene was dissolved in distilled water under ultrasonic. Then aqueous solution Cd-precursor ($CdCl_2$) was added drop-wise under stirring followed by drop-wise addition of aqueous solution of Na_2S. This resultant was stirred for 3 h. The resulting CdS–graphene composite was recovered by filtration, rinsed with deionized water several

times, and dried at 70 ^{o}C under vacuum. Morphology analysis confirmed that the obtained graphene-CdS photocatalyst was nanocomposite. Higher photocatalytic activity of this composite compare to bare CdS attributed to highly dispersion of graphene on CdS and improved interfacial interactions between the semiconductor and co-catalysts. Therefore, graphene efficiently accepted and transported electrons from the excited CdS and suppressed charge recombination resulting improved interfacial charge transfer processes.

2.6.4 Precipitation method

Peng et al. [199] reported the synthesis of GO–CdS by precipitation method. First, graphene oxide (GO) was synthesized by a modified Hummers' method. After that, typically, required amount of $Cd(Ac)_2 \cdot 2H_2O$ and exfoliated GO were added into water to obtain 0.1 M $Cd(Ac)_2$ solution. Then, 100 mL of Na_2S solution (0.11 M) was added drop-wise under stirring. The resultant mixture was continuously stirred for 1 h. After centrifugation, the product was washed with water and acetone and then dried at 313 K. GO−CdS composite shows a maximum H_2 production rate that was 1.5 times higher than bare CdS. Enhanced activity attributed to coupling of GO with the CdS nanoparticles. It could efficiently accept and transport electrons from the excited semiconductor, which suppressed the charge recombination and improved the interfacial charge transfer processes.

Wang et al. [200] prepared GO doped ZnS–CdS by precipitation method. First, GO was prepared by following the modified Hummer method. Then, in a typical process, required amount of GO solution was added to 50 mL of DI water with constant stirring. A predetermined amount of $Zn(CH_3COO)_2$ and $Cd(CH_3COO)_2$were added into

an aqueous solution of GO under constant stirring. Afterward, 50 mL of aqueous Na_2S solution was added drop wise with constant stirring for 1 h. The mixed solution was washed with DI water and vacuum dried at 333 K for 24 h. ZnS and CdS nanoparticles were loaded on the surface of GO nanosheets and formed a sheet-like morphology. The photocatalytic hydrogen generation rate of the ZnS–CdS/GO was approximately twice that of ZnS–CdS. Improved hydrogen production rate was attributed to high carrier transport property of GO nanosheets that constructed transport carrier channels between ZnS and CdS nanoparticles. It also enhanced the cooperative effects in the hetero-structure.

2.6.5 Hydrothermal/solvothermal method

Many workers have reported preparation of GO/rGO supported CdS by solvothermal or hydrothermal techniques.

Solvothermal method was used to synthesize graphene-CdS photocatalyst by Li et al., [201]. In preparation method, graphene oxide (GO), $Cd(Ac)_2$ as a Cd precursor & dimethyl sulfoxide (DMSO) as a solvent and sulphur source were used. The activity for hydrogen production increased 4.87 times rather than CdS alone. They demonstrated that graphene enhanced activity due to its properties as an excellent supporting material as well as collector and transporter of electron to separate photogenerated electron–hole pairs.

Zeng et al. [202] also prepared rGO–CdS by following hydrothermal method. In detail, Cd precursor, $Cd(Ac)_2.2H_2O$ was added with DMSO solvent containing GO. It was sonicated then this suspension was transferred into a Teflon-lined stainless steel autoclave for further solvothermal treatment at 453 K. They also prepared CdS and

RGO–CdS by a precipitation process for comparison. The activity for hydrogen production increased two times rather than CdS alone. Physical mixtures of rGO-CdS did not show enhanced photoactivity for H_2 evolution compared to CdS. Enhanced activity was reported due to implantation of rGO that played roles such as suppressing the photogenerated carrier recombination as an electron-transfer channel and acceptor, as well as support of CdS in aqueous solution.

Ye et al. [203] also prepared CdS–graphene nanocomposite following hydrothermal treatment. In which first, GO was dissolved in water under ultrasonic treatment for 1 h. Then, cadmium precursor ($Cd(Ac)_2$) was added. Subsequently, the aqueous solution of Na_2S was added drop-wise into this solution under constant stirring. Then it was put into a Teflon-lined autoclave at 453 K hydrothermal treatment. Hydrogen production rate was reported to be 4.8 times higher than CdS. They reported that CdS nanoparticles having the size of~35 nm were dispersed on the graphene sheets in the nano-composites. Significant band-gap narrowing was also reported due to the incorporation of graphene into CdS and showed the strong interactions between CdS and graphene.

Hong et al. [204] also prepared rGO-CdS by solvothermal method. In a typical process, GO was ultrasonically dispersed in the aqueous solution of DMF. Then Cd-precurosr $Cd(Ac)_2.4H_2O$ was added by following addition of TAA as sulphur source, and kept stirring for 0.5 h. This transparent solution was transferred into a Teflon-lined autoclave at 433 K for 24 h. They reported that hexagonal phase CdS and cubical phase CdS were formed by this method. Enhanced hydrogen production attributed to

formation of connection between CdS and GO, which exhibited a more efficient transfer of photoinduced electrons than mechanically loaded CdS.

Hou et al. [205] also prepared ternary composite CdS–$ZnIn_2S_4$–GO by hydrothermal treatment. In which commercially GO was ultrasonicated anhydrous ethanol solution for dispersion then as prepared CdS–$ZnIn_2S_4$was added. The constant stirring was done for to get homogeneous suspension. Then, transferred into Teflon-lined autoclave at 393 K. CdS–$ZnIn_2S_4$-GO showed about 4 times higher than that of the pure $ZnIn_2S_4$. They reported that three-dimensional architectures of CdS quantum dots incorporated in the porous assembly of marigold-like $ZnIn_2S_4$ heterostructures was achieved by following this preparation method. It led to enhanced hydrogen production with incorporation of GO. Hou et al. [206] also prepared CdS@TaON core shell composite embedded with GO as a cocatalyst. In the preparation of CdS@TaOn, an aqueous solution of Na_2S, nanoparticles of as prepared TaON were added cadmium acetate solution. The resulting yellow mixture was stirred for 24 h then was filtered. The wet solid was suspended in water (20 mL) and transferred to a Teflon lined stainless steel autoclave and put at 473 K for 72 h for hydrothermal treatment. Then it was dried at 368 K for 24 h under vacuum. This prepared CdS@TaON core shell was mixed with GO in ethanol solution. This mixing solution was put for ageing purpose under constant stirring to get homogeneous suspension. Then this suspension was put to a Teflon-lined autoclave at 393 K.

Leo et al. [207] also prepared CdS–rGO hybrid by following solvothermal method. Commercially GO was reduced by solvothermal method. Then, Cd precursor (Cadmium acetate), and sulphur precursor (thiourea) were mixed with

as prepared rGO in synthesis of hybrid. The autoclave was filled with this mixture and ethylenediamine. It was then put at 393 K for 12 h. Wrinkle and rippled shape structures were formed by this method. Hydrogen production was enhanced by 1.5 times compared to CdS, attributed to the highly crystalline structure, the crystal size, and the nature of the contact of CdS with rGO helped in the migration and transport of charges in the CdS-rGO hybrids.

Yu et al. [157] also prepared noble metal free CdS/MoS_2/Graphene hallows spheres. First GO was prepared by following modified Hummers method. Then CdS/MoS_2/graphene hybrids were prepared by one step hydrothermal method. In this process, first Cadmium acetate (Cd precursor) with GO was added into DI water, did sonication and then added cysteine (sulphur precursor) and sodium molybdate (Mo precursor) under constant stirring. This homogenous solution then transferred into auto clave and put at 573 K for 24 h. The unique hollow structures of composite and 2D graphene with high specific surface area were attributed to the high H_2 production activity as reported by them.

Cao et al. [208] prepared graphene-CdS nanowires by a solvothermal method. It resulted into high hydrogen evolution rate which was almost 2 times higher than that of bare CdS nanowires. Graphite oxide was firstly prepared by a modified Hummers method. Then GO was ultrasonically dispersed in ethylenediamine (EDA) followed by addition of $Cd(NO_3)_2.4H_2O$ and thiourea. This homogeneous solution was then transferred into a Teflon-lined autoclave which was then filled with EDA to 80% of the capacity and put at 433 K for 48 h. Enhanced hydrogen production rate attributed to the superb electron-conductivity of graphene as well surface area.

Xu et al. [209] prepared graphene–CdS composite by solvothermal process. rGO/CdS, rGO and $Cd(CH_3COO)_2 \cdot 2H_2O$ was added into DMSO. The suspension was transferred into a 100 mL Teflon-lined stainless steel autoclave. Then it was heated to 453 K and maintained for 12 h. Inhabitation of aggregation of the graphene sheets was reported by this group by following this preparation method. They reported that the heterojunction was formed between CdS and graphene that promoted electrons to transfer from CdS to graphene and reacted with protons on the active sites on graphene. Therefore, the recombination of the charge carriers was suppressed. The hydrogen production rate of the composite catalyst was 19.3 times higher than that of physical mixed sample.

Commonly, precursors of 'Cd' & 'S' and GO/rGO were dispersed ultrasonically and kept at elevated temperatures (150-200 ^oC) in an auto clave for a few hours. Apart from photocatalytic hydrogen production, many research groups [210–214] also prepared GO/rGO-CdS based photocatalyst by following hydrothermal/ solvothermal technique. These catalysts were used another photocatalytic application and showed improved photocatalytic activities compared to bare CdS.

On the basis of above discussion, it is concluded that GO/rGO can accept photogenerated electrons from the CBs of CdS, and further will efficiently prevent the recombination of photogenerated electron-hole resulting into improved photocatalytic H_2 production activity. One major responsible factor is its high work function (4.42 eV) [103]. Moreover, GO/rGO has high electronic conductivity, as a result the accepted electrons can easily move across its 2D plane to the surface for H_2 evolution. Therefore,

GO/rGO plays an efficient role of an electron acceptor and transporter. Further, for an efficient transfer of electron from CdS to GO/rGO to take place, the nature of interface plays a major role.

Table 2.2: GO/rGO-CdS based photocatalysts for H_2 production by dissociation of water.

Sr.	Photocatalyst	Preparation method	Sacrificial agents	Light source	H_2production ($\mu mol.h^{-1}$)	Ref
1.	rGO/CdS	In situ growth	-	-	-	Cao et al. 2011 [192]
2.	rGO/CdS-Pt	Solvothermal	Lactic Acid	350 W, Xe-lamp, $\lambda \geq 420$ nm	1120	Li et al., 2011[201]
3.	CdS/N-rGO	Sol-gel	Na_2SO_3, Na_2S	350 W, Xe-lamp, $\lambda \geq 420$ nm	50	Jia et al., 2011[197]
4.	CdS/rGO	Solvothermal	Na_2SO_3, Na_2S	300 W Xe-lamp $\lambda \geq 420$ nm	480	Zeng et al., 2011 [202]
5.	rGO/CdS	Two Phase	Methanol	400 W High-press. Hg lamp	110	Gao et al., 2012 [193]
6.	rGO/CdS	Precipitation	Na_2SO_3, Na_2S	300 W Xe-lamp $\lambda \geq 420$ nm	314	Peng et al., 2012 [199]
7.	CdS/rGO	Hydrothermal	Na_2SO_3, Na_2S	200 W Xe-lamp $\lambda \geq 420$ nm	70	Ye et al., 2012[203]
8.	CdS@TaOH-RGO-Pt	Hydrothermal	Na_2SO_3, Na_2S	NA Under Visible light irradiation	633	Hou et al., 2012[206]

9.	CdS/Al_2O_3 /RGO	Solid State	Na_2SO_3, Na_2S	500W, Phoenix tungsten halogen lamp	350	Khan et al., 2012 [196]
10.	CdS/ZnO /RGO	Solid State	Na_2SO_3, Na_2S	500W Phoenix tungsten halogen lamp	751	Khan et al., 2012 [196]
11.	CdS/graphene	Sol-gel	Na_2SO_3, Na_2S	300 W Xe-lamp, $\lambda \geq 420$ nm	5	Lu et al., 2012 [198]
12.	CdS QDs–$ZnIn_2S_4$/ GO	Hydrothermal	Na_2SO_3, Na_2S	300 W Xe-lamp, $\lambda \geq 420$ nm	2700	Hou et al., 2013 [205]
13.	CdS-MoS_2 /graphene	Hydrothermal	Lactic Acid	500 W	1800	Jia et al., 2014 [195]
14.	CdS-ZnS-GO	Precipitation	Na_2SO_3, Na_2S	300 W, Xe lamp $\lambda \geq 420$ nm	750	Wang et al., 2015 [200]
15.	CdS- graphene	Hydrothermal	Na_2SO_3, Na_2S	350 W, Xe Arc lamp $\lambda \geq 420$ nm	800	Li et al., 2015 [201]
16.	Graphene-CdS	Solvothermal method	Na_2SO_3, Na_2S	300 W, xenon lamp	1344	Cao et al., 2015 [208]
17.	rGO-CdS	Solvothermal method	$(NH_4)_2SO_3$	300 W,, Xe-lamp	1400	Hong et al. 2015 [204]
18.	Graphene–CdS	Solvothermal process	Na_2SO_3, Na_2S	300 W, Xenon lamp	175	Xu et al., 2016 [209]
19.	CdS-MoS_2 /graphene	Solvothermal method	Lactic acid	300 W, xenon lamp $\lambda \geq 400$ nm	1913	Yu et al., 2016 [157]

20.	CdS/rGO	Two phase	Triethanol amine	300 W, Xe arc lamp	4800	Tonda et al., 2017 [194]
21.	rGO-CdS	Solvothermal method	Na_2SO_3, Na_2S	150 W, Xe arc lamp	3.85	Leo et al., 2017 [207]

2.7 Role of sacrificial agents

Fig. 2.17 shows different schemes of photocatalytic water dissociation. Energy levels of photocatalysts and the redox potential of water are shown in the diagram.

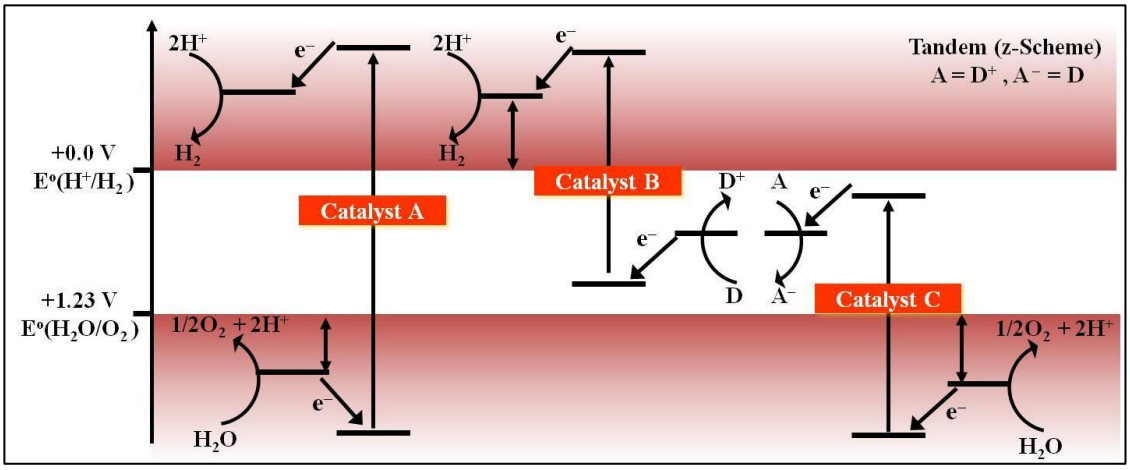

Figure 2.17: Energy scheme for photocatalytic water splitting

First case (A) is the single absorber case, CB edge and VB edge are proper positioned for both hydrogen and oxygen production. Because conduction band edge is more negative and valence band edge is more positive with respect to water redox potentials, therefore, simultaneously both hydrogen and oxygen production can take place in a single cell [215–218].

In second case (B), the conduction and valence band positions qualify only for the water reduction, and it requires are reducing agent to satisfy photogenerated holes to enable photocatalytic hydrogen production. In third case (C), i.e. generally the photo anode case, positions are qualifying only for the water oxidation. There is a requirement of chemical oxidant to extract the photogenerated electrons. Thus photocatalysts B and C will require sacrificial agents to satisfy photogenerated holes and electrons, respectively. These two (catalyst B and catalyst C) are combined in series to split one molecule of water after absorbing four photons. That is a typical z-scheme configuration.

In the present study, we focus on hydrogen production (case B) which requires a sacrificial agent in the solution which provides electron to the valence band of photocatalyst to satisfy holes.

A common sacrificial agent is the mixture of S_2^{2-} / SO_3^{2-} [219]. The basic principle and steps involved in photocatalytic reactions for hydrogen production using electron donors/acceptors as the sacrificial reagents is depicted in equations 2.2 to 2.6[139, 220, 221]:

$$\text{Photocatalyst} + h\nu \rightarrow h^+ + e^- \quad (2.2)$$

$$2e^- + 2H_2O \rightarrow H_2 + 2OH^- \quad (2.3)$$

$$2S^{2-} + 2h^+ \rightarrow S_2^{2-} \quad (2.4)$$

$$S_2^{2-} + SO_3^{2-} \rightarrow S_2O_3^{2-} + S^{2-} \quad (2.5)$$

$$SO_3^{2-} + S^{2-} + 2h^+ \rightarrow S_2O_3^{2-} \quad (2.6)$$

In addition the following reaction may also take place:

$$SO_3^{2-} + 2OH^- + 2h^+ \rightarrow SO_4^{2-} + 2H^+ \quad (2.7)$$

Therefore, in the presence of an electron donor, the photogenerated holes irreversibly oxidize the reducing electron donors.

Photogenerated holes are powerful oxidizing agent and can cause photocorrosion of CdS leading to its deactivation. However, if suitable electrolytes as sacrificial agents are present in the solution, they consume holes and the life of catalyst remains unaffected.

Presence of sulphide ions in the electrolyte also prevents photocorrosion of CdS [222] by the reaction given below and thus enhances its life:

$$CdS + h\nu \rightarrow h_{VB}^{+}(CdS)^{+} + e_{CB}^{-}(CdS)^{-} \quad (2.8)$$

However, reaction 2.8 is completed by the reaction:

$$h_{VB}^{+}(CdS)^{+} + CdS \rightarrow Cd^{2+} + S^{2-} \quad (2.9)$$

Which is responsible for the photocorrosion of CdS.

When sulphide ions are present, holes are preferably satisfied by the reaction:

$$h_{VB}^{+}(CdS)^{+} + S^{2-} \rightarrow S_2^{2-} \quad (2.10)$$

$$h_{VB}^{+}(CdS)^{+} + S^{2-} \rightarrow S \quad (2.11)$$

$$S + S^{2-} \rightarrow S_2^{2-} \quad (2.12)$$

In the presence of sulphide ions, photogenerated holes are reacted with sulphide ions to form either sulphur or disulphide ions instead of oxidizing CdS [223,224].

However, the colour of disulphide ions is yellow, which acts as an optical filter for photon and reduce the light absorption by CdS [225–227]. Sulphite ions are added as a sacrificial agent to overcome this problem. Sulphite ions react with disulphide ions to form thiosulphate ions. Reaction steps are as following:

$$S_2^{2-} + SO_3^{2-} \rightarrow S_2O_3^{2-} \quad (2.13)$$

These thiosulphate ions are colourless and do not create any obstacle into absorption of solar light by CdS.

2.8 Kinetics of photocatalytic dissociation of water

In addition, to the development of efficient and durable photocatalyst, design of a photoreactor which provides for an efficient adsorption of solar radiation is also a challenge. The kinetics of dissociation of water must be known for the design of a photoreactor. Surprisingly not much work has been reported in the literature on the mechanism and kinetics of the reaction. Working on CdS based catalysts with Na_2S alone or in combination with Na_2SO_3 as sacrificial agents; it has been reported [228–230] that rate of hydrogen production declines after sometime and eventually becomes zero. The deactivation of CdS catalyst was concluded to be the reason of fall in the hydrogen production rate. Kinetics studies have been reported in the literature but all have focused on initial rate determination and mechanism of the reaction.

Matsumura et al. [140] reported the decrease in rate of H_2 production with time which was attributed to the decrease in the concentration of sulphite ion and change in pH.

Bühler et al. [220] carried out the experiment with different donor species. The reaction rate was reported to decrease due to decreasing concentration of SO_3^{2-} when only sodium sulphite was used as a donor. However, when sodium sulphide was used as a donor; it formed yellow disulphide (S_2^{2-}) ions after reacting with holes. Coloured disulphide prevented the light to reach to the photocatalyst surface. They have also

reported that the decrease in the rate was less 21% after six days when a mixture of sulphide and sulphite was used with maintaining concentration throughout.

Furlong et al. [231] have reported the loss of rate due to (a) consumption of donor and (b) loss of catalyst activity by hydrogen produced during irradiation. Further Furlong and his co-workers [232] also presented kinetic model for H_2 production by dissociation of water in presence of Na_2S using Pt-CdS photocatalyst.

The following steps of reaction have been proposed:

$$R^* + HS^-_{ads} \rightarrow S^- + H\cdot (+R^*) \quad (2.15)$$

$$R^* + S^- + H_2O \rightarrow S^o + H\cdot (+R^*) + OH^- \quad (2.16)$$

$$H\cdot + H\cdot \rightarrow H_2 \quad (2.17)$$

Where, R^* is a steady state 'reactive entity' which may be indentified with the photogenerated electron-hole pairs and HS^- ads is the quantity adsorbed on to CdS. It is given by:

$$[HS^-]_{ads} = \frac{K_L[HS]^-_{aqs}Ns}{1 + [HS]^-_{aqs}} \quad (2.18)$$

Where, K_L is the Langmuir adsorption constant and *Ns* is the concentration of surface sites available for adsorption ($mol^{-1}.dm^{-3}$).

Sebate et al. [233] have proposed the following general steps in the photo-production of hydrogen with sulphide and sulphite mixtures:

Step 1, absorption of photon:

$$CdS + h\nu \rightarrow CdS + h^+ + e^- \quad (2.19)$$

Step 2, reaction on the catalyst surface:

Cathodic: $2H_2O + 2e^- \rightarrow H_2 + 2OH^-$ (2.20)

Anodic: $2HS^- + OH^- + 2h^+ \rightarrow HS_2^- + H_2O$ (2.21)

Step 3, reaction in the liquid phase:

$HS_2^- + SO_3^{2-} \rightarrow S_2O_3^{2-} + HS^-$ (2.22)

Global reaction:

$HS^- + SO_3^{2-} + H_2O \rightarrow H_2 + S_2O_3^{2-} + OH^-$ (2.23)

Absorption of reactants:

$C + HS^- \rightarrow C - SH^-$ (2.24)

$C + OH^- \rightarrow C - OH^-$ (2.25)

$C + SO_3^{2-} \rightarrow C - SO_3^{2-}$ (2.26)

Reaction on the catalyst surface

Cathodic reaction:

$C - SH^- + C + e^- \rightarrow C - S^{2-} + C - H^{\cdot}$ (2.27)

$2C - H \rightarrow 2C + H_2$ (2.28)

Anodic reaction:

$C - SH^- + h^+ \rightarrow C - SH^{\cdot}$ (2.29)

$C - OH^- + h^+ \rightarrow C - OH^{\cdot}$ (2.30)

$C - SH^- + C - OH^{\cdot} \rightarrow C - SH^{\cdot} + C - OH^-$ (2.31)

$C - SH^{\cdot} + C - OH^- \rightarrow C + C - SH^{\cdot -} + H_2O$ (2.32)

$C - SH^{\cdot} + C - S^{\cdot -} \rightarrow C - S_2H^- + C$ (2.33)

Desorption of products

$C - S_2H^- \rightarrow C + HS_2^-$ (2.34)

Adsorption of thiosulphate and reverse reactions:

$C + S_2O_3^{2-} \rightarrow C - S_2O_3^{2-}$ (2.35)

$C - S_2H^- + H_2O + 2e^- \rightarrow C - SH^- + HS^- + OH^-$ (2.36)

$$C - S_2O_3^{2-} + H_2O + 2e^- \rightarrow C - SH^- + SO_3^{2-} + OH^- \quad (2.37)$$

The symbol C represents active sites of catalysts. Say, Cd^{2+} ion on the catalyst surface, where negatively charged species can be adsorbed. Two possibilities were considered for the anodic reactions on the catalyst surfaces. The hole could be captured by an adsorbed OH^- (Eq^n. 2.30) or adsorbed HS^- (Eq^n.2.29). In the first case reaction Eq^{n}s. 2.31-2.33 would be occur after reaction Eq^n. 2.30. If the hole is captured by an adsorbed on the catalyst surface and thereby block active sites (Eq^n. 2.35). The adsorbed polysulphide and thiosulphate can complete with protons for the capture of electrons in terms of the reverse reaction Eq^{n}s.2.36 and 2.37, respectively. In their experiments, alkaline solution of H_2S and SO_2 was used, in which CdS was suspended. This photocatalytic reaction led to the production of H_2 and thiosulphate. The variation of the reaction rate in response of various parameters such as loading of photocatalyst, concentration of sacrificial agents (sulphide ions and sulphite ions), thiosulphate ions, pH and temperature were studied. Langmuir-Hinshelwood-Hougen-Watson model was successfully applied to analyze the kinetic data. In which, surface reaction related to an anodic type reaction was reported to be the rate controlling step. Further work has been reported by Sebat et al [234]. They have reported that three factors were involved in decrease of rate (i) reactant consumption, (ii) back reaction of products, and (iii) catalyst deactivation. They also proposed that the promotion of electrons to the conduction band brings about a change in the catalyst surface and the nature of bonding at the displacement site. These changes, not being instantaneous, lead to an induction period in the activity profile. Secondly, the reactant adsorption equilibria in the dark condition may not match with that in the illuminated condition and the re-equilibration process would require a finite time. Lastly, some oxygen might be left in the solution even after

purging with an inert gas and its reduction might compete with water reduction as following:

$$O_2{}^{2-} + 2H_2O + 2e^- \rightarrow 4OH^- \quad (2.38)$$

$$2H_2O + 2e^- \rightarrow H_2 + 2OH^- \quad (2.39)$$

Subrahmanyam et al. [235] stated only that hydrogen production rate could increase when product hydrogen was removed continuously from the system.

In an earlier work carried out in our laboratory with CdS based catalyst and sodium sulphide & sodium sulphite as sacrificial agents, a detailed kinetic study was reported [230]. The rate was found to be related to sulphide ions adsorbed on the surface of CdS. The decrease in the rate of H_2 production was concluded to be due to the deactivation of catalyst by the product hydrogen itself. The rate of adsorption of sulphide ions on the catalyst was reported to follow Elovich equation $[\frac{dq}{dt} = a'\exp(-bq)]$. A power law type ($R_{H_2} = kq^n a$) of rate expression was proposed for hydrogen evolution which also took into account the catalyst deactivation. Final expression was shown as:

$$\ln(R_{H_2}) = \ln(kq) - k'_d t \quad (2.40)$$

And the integrated form of the Elovich equation was:

$$q = \ln \frac{[a'bt+1]}{b} \quad (2.41)$$

Where, R_{H_2}– the rate of hydrogen production, *k* is the rate constant, *n* is the order of the reaction, $a[a = \exp(-k'_a t)]$is the fractional activity of the catalyst at any time *t*. The fractional activity (a) can be defined as the ratio of rate at any time to rate on fresh catalyst, k_d is the deactivation rate constant, *m* is the hydrogen production dependency factor, *d* is order of deactivation.

2.9 Enhancement in hydrogen production rate by ultrasound

Recently, ultrasonic mediated reactions i.e. also called sonocatalysis have been receiving special interest. Application of ultrasound in photocatalytic reaction has increased the photocatalytic efficiency. In the following pages we describe the principle of ultrasound waves and their application in enhancement in the photocatalytic reactions.

2.9.1 Theory and fundamentals

Ultrasonic waves (occurs at frequencies above 20 kHz) are a branch of sound waves and it exhibits all the characteristic properties of sound waves [236]. Depending on the frequency, ultrasound is divided into three categories, namely power ultrasound (20–100 kHz), high frequency ultrasound (100 kHz–1 MHz), and diagnostic ultrasound (1–500 MHz). Ultrasound ranging from 20 to 100 kHz is useful in chemical processes, in which chemical and physical changes as desired may take place due to cavitation of bubbles [237,238]. Ultrasound ranging from 1 to 10 MHz is used for animal navigation and communication, detection of cracks or flaws in solids, and under water echo location, as well as diagnostic purposes [as shown in Fig. 2.18 [239]].

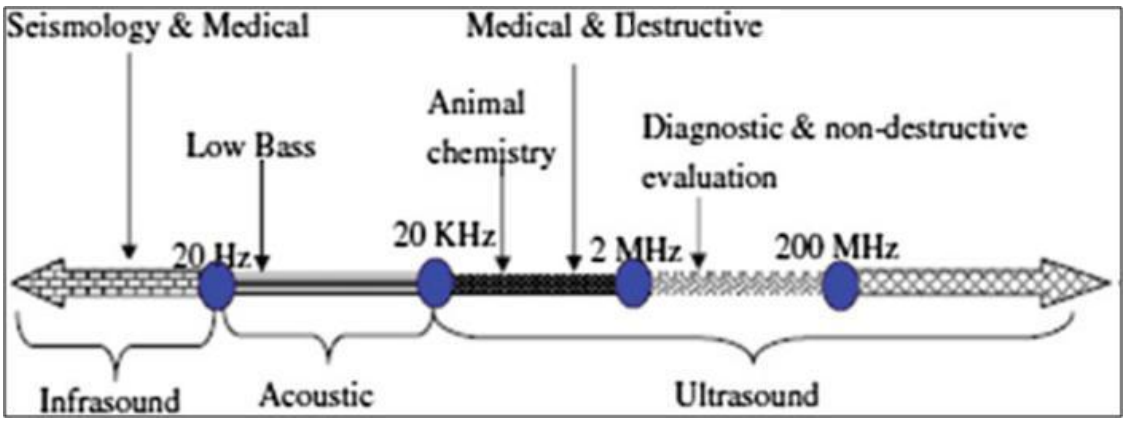

Figure 2.18: Diagram of ultrasound range.

The common term 'sonicated' is used in all places, generally describes a phenomenon when a fluid is subjected to power ultrasound which can also produce cavitation bubble. The cavitation bubbles produced from the ultrasound undergo very violent collapse within the fluid generating 'hotspots' of high energy within the fluid.

When applied on liquid, ultrasound waves which consist of a cyclic succession of expansion (rarefaction) and compression phases impart mechanical vibration. Compression cycles exert a positive pressure and push the liquid molecules together, while expansion cycles exert a negative pressure and pull the molecules apart.

When pressure amplitude exceeds the tensile strength of liquid in the rarefaction regions, small vapor–filled voids called cavitation bubbles are formed [240]. Generally, pure liquids possess great tensile strengths and thus, available ultrasonic generators are unable to produce high enough negative pressures to cause cavitation. However, most of the liquids are usually impure and its tensile strength is reduced due to the presence of numerous small particles, pre-existing dissolved solids, and other contaminants. The impurities in liquid represent weak points in a liquid where nucleation of cavitation bubbles will occur [241]. For instance, when pure water is used, more than 1,000 atm of negative pressure would be required for cavitation whereas for tap water, only a few atmosphere of pressure would be sufficient to form bubbles [242]. Once a bubble is created, two different cavitation phenomena which could take place in the liquid are: stable or transient cavitation. In stable cavitation, bubble wall couples with the acoustical field and oscillates about the equilibrium radius for several cycles. This occurs at low acoustic intensities, where the size of the bubble oscillates in phase with expansion and compression cycles and the bubbles grow slowly over many acoustical cycles [243]. Due

to its small variation in bubble size, this process is of little significance in terms of chemical effects [244]. The process is also called rectified diffusion as during expansion, water vapor; dissolved gases and organic vapor will enter the bubble and will leave during contraction because of the effect of bubble surface area [245]. When high intensity acoustic field is introduced, transient cavitation usually occurs. This causes growing cavitation bubble to eventually become unstable after a number of cycles and collapse during the compression cycle of ultrasonic wave. In this cavitation phenomenon, the size of a bubble drastically increases from tens to hundreds of times the equilibrium radius before it collapses violently in less than a microsecond [246,247]. In summary, phenomenon of cavitation consists of the repetition of three distinct steps: formation (nucleation), rapid growth (expansion) during the cycles until it reaches a critical size, and violent collapse in the liquid as shown in Fig. 2.19 [248]. Cavitation serves as a mean to concentrate the diffused sound energy. Upon collapsing, each of the bubble would act as a hotspot, generating energy to increase the temperature and pressure up to 5,000 K and 500 atm, respectively, and cooling rate as fast as 109 K/s. These collapsing bubbles create an unusual mechanism for high-energy chemical reactions due to enormous local temperatures and pressure [248].

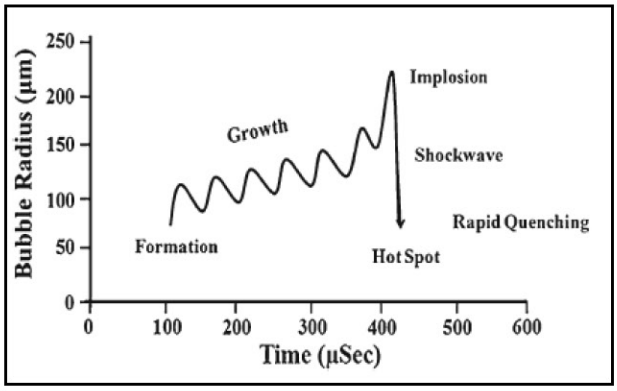

Figure 2.19: Growth and collapse of cavitation bubbles in aqueous solution under ultrasonic irradiation [248].

Besides chemical effects, ultrasound can also produce significant physical effects (sonophysical). When ultrasound is introduced, liquid medium will absorb the acoustic energy from sound waves and flow along the wave's propagation direction. Physical effects such as microstreaming, microstreamers, microjets, and shock waves can also be produced by cavitation bubbles, resulting in turbulent fluid movement and a microscale velocity gradient in the vicinity of cavitational bubbles [240,243].

The fluid movement produced by ultrasound could enhance the mass transfer processes between solid-bulk and gas-bulk interfaces. Hence, these sonophysical effects described above can facilitate various mixing, breaking down of particles and macromolecules, polymer degradation, desorption, extraction, and cleaning processes [240,243,248,249].

2.9.2 Application of ultrasound

For many years, Ultrasound has been applied in various processes such as cleaning, deaggregation of powder, emulsification, sterilization, extraction, plastic welding, dissolution, flotation, degassing, soldering, defoaming, drilling, filtration, homogenization, biological cell disruption, and crystallization as a stimulus of chemical reactions. This interest in the utilization of ultrasound is getting primarily due to its economical point of view, simple apparatus requirements, and low-severity condition i.e. can be operated at ambient conditions.

Initially, sonochemical degradation methods were used as a source of ·OH for treatment of organic pollutants. Sonolysis was reported as a feasible method for the mineralization and decolourization of dyes [250,251]. Although, most of the dyes were decolorized and mineralized, but rates were slow in practical uses. Therefore, catalysts

and adsorbent materials were added with ultrasound to enhance mineralization and degradation rates [252].

Many research groups [253–256] studied the degradation of dyes using ultrasound with addition of iron particles and reported enhanced dye degradation. Enhanced rate were attributed to (i) the increase in metal surface area due to the pitting and cracking effect of ultrasound on the metal surface, (ii) the continuous cleaning of the reactive surface by the shockwave and micro-jets that form during cavitational collapse and removal of the precipitation of iron oxides/hydroxides from the iron surface, and (iii) the increased mass transfer.

Hamdaoui et al. [257] reported that the cavitational effect on the adsorption process is caused by acoustic micro-streaming, which enhances mass and heat transfer at interfacial films surrounding adsorbent particles and within the pores. Additionally, the intra-particle diffusion coefficient which controlled adsorption processes also increased up to 3.6 times when coupled with ultrasound.

Ultrasonic irradiation was also used to pre-treat the Congo red solution followed by a biological treatment using Bacillus sp. isolated from the tannery industry. Pre-treatment with ultrasound reduced the power consumption and cost by reducing biodegradation time [258]. Liu et al. [259] studied effect of ultrasound on biodegradation process. They reported that the effect of ultrasonic irradiation on biodegradation could be assessed by following two reasons: (i) the facilitation of substrate diffusion and (ii) the enhancement of cell enzyme secretion. Additionally, the formation of ultrasonic cavitation could promote particle movement in reaction solution and thus, accelerate mass transfer in the reactor and enhance the permeability of cell

membrane and wall around cavitation bubbles. Applications of ultrasound were also reported in the intensification of leaching process [260] and enzyme processing [258,261].

Lorimer et al. [262] used ultrasound in electrochemical processing. They reported potential advantages of ultrasound are: (i) ultrasonic degassing at an electrode surface prevents gas bubble accumulation, which interferes with the passage of current; (ii) agitation via cavitation at the electrode surface assists in ion transport through the diffusion layer; and (iii) cavitation at the electrode surface results in continuous cleaning and activation of the electrode.

Researchers have used ultrasound technique widely in the area of advanced oxidation process [248,263–266]. Combination of ultrasound with advanced oxidation processes enhanced the degradation rate compared to either method applied alone. In these processes, treatment of contaminants in water was successfully performed without need of extreme physical conditions. The reasons attributed for these improvements were turbulence created in the liquid due to ultrasound which reduced the mass transfer resistance and also increased the surface area available for photocatalysis.

Several studies also postulated synergy between photocatalyst and ultrasound in which the combined efficiency is more than the sum of the efficiencies for the individual processes in few cases. Mason et al. [267,268] reported that the use of ultrasound into a photocatalytic reaction system might enhance mass transport and catalytic activity due to surface cleaning and particle size reduction. Ultrasound might also modify the rate of photocatalytic degradation by promoting the deaggregation of the catalyst. This increased its active surface area, and thereby the amount of reactive

radical species through cavitations and ultimately enhanced degradation/mineralization of the pollutant. Adewuyi et al. [269] have made an extensive overview of different studies on the use of sonophotocatalysis for treatment of wastewaters. Berberidou et al. [270] observed that the degradation of Malachite Green (MG) in water by TiO_2 sonophotocatalysis was faster than the respective individual process which was attributed to the enhancement of formation of reactive radicals as well as the increase in the active surface area of the catalyst. The hybrid effect of the irradiation by light and ultrasonic waves in conjunction with H_2O_2 was first confirmed by Yano et al. [271]. Kulkarni et al. [272] reported that photocatalysis combined with ultrasound yields higher degradation rates of the contaminants. This is explained based on the standard effects of ultrasound on photocatalyst: i.e., the mechanical effects of cavitations involving photocatalyst surface cleaning and increased mass transfer of the polluting species to the powdered catalyst surface.

The effectiveness of sonophotocatalysis in the degradation/mineralization of pollutants can be attributed to the following: (i) ultrasound provides an extra source of ·OH radicals through cavitation; (ii) acoustic cavitation can remove intermediates from the photocatalytic active sites and make the sites available for fresh adsorption and activation. It causes a number of physical effects, such as shear forces, turbulence and micro-streaming that helps to regenerate the active catalytic surface. It may enhance mass transfer towards the liquid–solid interface and accelerate the rate of adsorption of reactant on the photocatalyst. Sonolysis is likely to decompose the hydrophobic part of the pollutant compound, which is unlikely to occur on the surface of the photocatalyst.

Anju et al. [273] and Chen et al. [274] also postulated that during photocatalysis reaction products and other intermediates might remain attached on the photocatalyst

surface resulting in a lower activity due to unavailability of these surfaces for further adsorption of solar radiation. Ultrasound detached these from surface and provided for photons adsorption. However it may be in order to mention that Chakma et al. [275] have reported adverse effect of ultrasound on the oxidation of dye by photocatalysis. They reported that shock wave generated by cavitation bubbles resulted into desorption of dye molecules adsorbed on the surface of photocatalyst.

A few works have been reported in literature on the synergetic effect of ultrasound on photocatalytic dissociation of water for hydrogen production.

Harada et al. [276] reported enhanced efficiency of sonophotocatalytic reaction in water splitting using TiO_2 photocatalyst. Experiment was performed in a Pyrex glass bulb containing the photocatalyst (TiO_2) suspended in distilled water subjected to simultaneous irradiation from one side with a 500 W Xe lamp and from the bottom with a 200 W ultrasonic generator (200 kHz).In this experiment, liquid water was decomposed to hydrogen and oxygen by sonophotocatalysis. Later, Harada and his co-workers [277] also reported overall water splitting using sonophotocatalysis in presence of CO_2+Ar atmosphere. Simultaneous irradiation was performed from one side of the reactor using a 500 W xenon lamp and from the bottom of the reactor using a 200 W ultrasonic generator in a CO_2–Ar atmosphere at 25 °C. The reactor was placed in a Pyrex bath with a temperature controller during the reaction.TiO_2 was used as a photocatalyst.

Gentili et al. [278] have reported that the combined effect of electromagnetic (of light) and mechanical (of ultrasound) waves enhanced mass transport and consequently rate. They presented experimental work by using ethanol as sacrificial reagent,

$S:La_{0.8}Ga_{0.2}InO_3$ as catalyst and ultrasounds, generated by 38 kHz and 50 W piezoelectric transducer, light source 35 W Xe lamp. Hybrid action of light and ultrasounds remarkably increased the H_2 production.

Penconi et al. [279] reported the study of hydrogen production from a water/ethanol mixture in the presence of heterogeneous catalyst by using combination of UV-visible electromagnetic radiation and ultrasound waves. They carried out the experiments of sonolysis and sonophotolysis by irradiating 300 mL of a ethanol/water solution with ultrasound waves of 38 kHz frequency, at the maximum intensity of irradiation, and in the presence of of $S:Y_{0.8}Ga_{0.2}InO_3$. Interesting synergetic effect of these two types of energies ultrasound and irradiation was reported on hydrogen production. Overall, ultrasound can enhance chemical reactions. Therefore, an ultrasonic process combined with other technique can be promising way for the degradation of organic pollutants as well as other photocatalytic processes. Photocatalysis with ultrasound can be considered an attractive, effective process for enhanced photocatalytic hydrogen production by dissociation of water under solar radiation.

2.10 Future scope of work based on the literature review

Hydrogen has all the attributes to be considered as the future source of energy. It becomes more attractive when hydrogen is produced by dissociation of water utilizing the solar radiation. To this effect photocatalytic decomposition is a promising technology. The major cost of any such set-up will be those of photoreactors. However, size and consequently the cost of photoreactor can be reduced if efficient photocatalysts are developed. Therefore, extensive work has been reported in the literature on the development of photocatalysts.

There are two classes of catalysts, i.e. oxides and chalcogenides. Chalcogenides are inherently more active and have narrow band gap suitable for harvesting of solar radiation. Conduction band edges of these compounds are more negative compared to the reduction potential of water and thus making reduction of water feasible. Cadmium sulphide is one such photocatalyst. However, CdS suffers from photocorrosion. Literature reports that the photocorrosion may be suppressed by using appropriate sacrificial agents.

However, the charge recombination (recombination of photogenerated electrons and holes) has no easy solution. Two approaches have been reported in the literature. In the first approach a noble metal, especially Platinum is incorporated in the semiconductor and the metal acts as a sink for electron. In the second approach, a composite is made of two semiconductors where photogenerated electrons in semiconductor of narrow band gap are transferred to the conduction band of the large band gap semiconductor. Catalysts have been developed using both the approaches. Owing to the high cost of noble metals the second approach is being investigated.

The transfer of electron from one semiconductor to another depends on the nature of interface between the two semiconductors. A chemical interaction which leads to an intimate contact between the two is essential. Therefore, development of catalyst preparation techniques which results into an appropriate microstructure for high activity is a contemporary area of research. There are many semiconductors which have been attempted with CdS. However, recently there is a focus on the use of GO/rGO as cocatalyst with CdS. GO/rGO has many positive attributes. Its semiconductor property

can be tailored by doping, these have excellent electron mobility property and they can also chemically interact with CdS at the interface to promote efficient charge separation For the designing of a photoreactor, the kinetics of reaction must be known. However, not much work has been reported on the kinetics of reaction. Further, there are reports that catalysts deactivate with time however, detailed mechanism of deactivation and kinetics of activation/deactivation are not well documented.

Intensification of photocatalytic processes have also been reported with the help of ultrasound in particular for photo-oxidation of pollutants. However, there are only few studies on the effect of ultrasound on the photocatalysis of water for hydrogen production.

2.11 Objectives of present work

The present work was carried out with the following objectives:

- Develop an active GO/rGO–CdS based photocatalysts for hydrogen production by photocatalytic dissociation of water utilizing solar radiation.
- Carry out detailed characterization of photocatalysts to understand microstructure of catalysts.
- Establish a relation between variables of preparation of catalysts, catalyst microstructure and activity.
- Study the kinetics of reaction and activation & deactivation of catalysts.
- Study the effect of ultrasound on photocatalytic hydrogen production rate.